Circadian rhythm disruption alters mammary gland morphology and accelerates "cold" aggressive tumorigenesis through a LILRB4-dependent pathway.

Short title: Circadian disruption causes tumorigenesis via LILRB4

Authors

Olajumoke Ogunlusi,[1†] Mrinmoy Sarkar,[1†] Arhit Chakrabarti,[2] Devon J Boland,[3] Tristan Nguyen,[1] James Sampson[4], Christian Nguyen,[1] Danielle Fails,[5] Yava Jones-Hall,[6] Loning Fu,[7] Bani Mallick,[2] Alex Keene,[1] Jeff Jones,[1] Tapasree Roy Sarkar[*1]

Affiliations

[1]Department of Biology, Texas A&M University, College Station, TX, USA.

[2]Department of Statistics, Texas A&M University, College Station, TX, USA.

[3]Texas A&M Institute of Genome Sciences & Society (TIGSS), College Station, TX, USA.

[4] Department of Biomedical Engineering, Texas A&M University, College Station, TX, USA.

[5]Fortis Life Sciences, Montgomery, TX 77356, USA.

[6]Veterinary Pathobiology, Texas A&M University, College Station, TX, USA.

[7]Baylor College of Medicine, Houston, TX, USA.

[*]**Corresponding author:** tsarkar@bio.tamu.edu.

[†] These authors contributed equally to this work.

Abstract

Epidemiological studies have shown that circadian rhythm disruption (CRD) caused by shift work or frequent jet lag is associated with the risk of breast cancer development. However, the role of CRD in mammary gland morphology and aggressive mammary tumorigenesis and the molecular mechanisms underlying CRD and cancer risk remain unknown. We found that chronic CRD disrupted mouse mammary gland morphology and increased tumor burden and lung metastasis in a genetically engineered mouse model of aggressive breast cancer and induced an immunosuppressive tumor microenvironment by enhancing leukocyte immunoglobulin-like receptor 4a (LILRB4a or LILRB4) expression. Moreover, CRD increased the M2 macrophage (anti-inflammatory) and regulatory T-cell populations but decreased the M1 macrophage (proinflammatory) populations. These findings identify and implicate LILRB4a as a link between CRD and aggressive mammary tumorigenesis.

Teaser

Circadian rhythm disruption enhances aggressive mammary tumorigenesis by elevating LILRB4a expression.

Introduction

The circadian clock regulates the expression of several genes that impact physiology, metabolic processes, and health outcomes (*1-3*). Epidemiological studies have reported that circadian rhythm disruption (CRD), such as that which occurs during shift work or travel across time zones, affects human health and increases the risk of developing cancer, metabolic disorders, and cardiovascular disease (*4*). According to the National Health Interview Survey, 12–35% of the US population works irregular schedules, including night and rotating shifts (*5*). CRD increases the risk of different types of cancer, including lung (*6, 7*), colon (*8*), and breast(*9, 10*) cancers.

Breast cancer is the second-most common cancer among women worldwide (*11*). Shiftwork was found to increase the incidence of breast cancer in nurses by approximately 50%, suggesting a critical role for the circadian clock in breast cancer pathogenesis (*12*). Circadian clocks regulate the rhythmic expression of numerous genes in breast tissues (*11*). Triple-negative breast cancer (TNBC) or basal phenotype (*13*) encompasses a breast tumor subtype that is clinically negative for the expression of the estrogen (ER) and progesterone (PR) receptors and lacks overexpression of the Human Epidermal Growth Factor Receptor 2 (HER2) protein, with unique prognostic and therapeutic implications (*14*). TNBC is responsible for more than 15–20% of all breast cancers, with a mortality rate of 40% (*15*). TNBC is relatively aggressive and shows more resistance to chemotherapy than other subtypes of breast cancer (*15*). Although modern technologies, including next-generation sequencing, allow visualization of the genomic landscape and genetic events of TNBCs, the impact of CRD on aggressive TNBCs remains unknown. Therefore, understanding the role of circadian disruption in aggressive mammary tumorigenesis is critical for developing novel therapeutics.

The suprachiasmatic nucleus (SCN) in the anterior hypothalamus influences the peripheral clock (which regulates numerous physiological processes, including cell proliferation and apoptosis) and the central clock via a combination of neural and hormonal signals (*16*). The molecular basis of both the central and peripheral clocks is the interaction of positive and negative feedback loops governed by clock proteins (*17*). In the primary feedback loop, the "positive elements" CLOCK and BMAL1 heterodimerize through their PAS domains and activate the transcription of target genes that contain an "E-box" in their promoter regions. Once they activate the transcription of the "negative elements," i.e., the period genes *Per1* and *Per2* and the cryptochrome genes *Cry1* and *Cry2*, the PER/CRY heterodimers inhibit the transcription of their gene(s) by blocking CLOCK/BMAL1-dependent transactivation (*1*). This feedback loop regulates the transcription of an estimated 30% of the genome (*18*). The expression of core circadian clock genes is frequently dysregulated in human tumors, indicating the tumor-suppressive role of the molecular clock (*8, 19, 20*). For example, Per2 plays an essential role in mammary gland development, and individuals with mutations in the core clock genes have an increased prevalence of breast cancer (*17*). Therefore, molecular dysfunction of both the core circadian clock in the SCN, or circadian transcriptional rhythms in breast tissue promotes breast cancer pathogenesis. Epidemiological studies have also emphasized that the risk of developing cancer increases with increasing years of shift work (*21*), indicating that longitudinal experiments are better suited for characterizing how CRD may affect tumorigenesis.

Here, we investigated how the loss of circadian function impacts mammary glands, tumorigenesis, and the tumor microenvironment (TME). Studies have demonstrated the critical role of clock components in regulating several processes, such as cell proliferation, DNA repair, and cell death, abnormalities linked to cancer. In this study, we aimed to investigate the impact of CRD on mammary glands using an immunocompetent mouse model and the impact on tumorigenesis and

the tumor microenvironment (TME) using an aggressive basal or TNBC mouse model. To this end, we used the jet lag schedule, which mimics the circadian disturbance humans encounter during rotating shift work or frequent jet lag, and the genetically engineered mouse model (GEMM) of TNBC. We specifically examined the role of leukocyte immunoglobulin-like receptor 4a (LILRB4a or LILRB4 or gp49B), which is known to suppress immunity in acute myeloid leukemia (AML) and solid tumors (*22, 23*). Additionally, we investigated whether the elevation of LILRB4 expression could be a key molecular event in CRD-induced mammary tumorigenesis and immunosuppressive TME. Overall, this study provides a better understanding of how circadian desynchronization affects mammary gland morphology, aggressive mammary tumorigenesis, and identifies a compelling target for immunotherapy of CRD-induced tumorigenesis.

Results

Chronic CRD interrupts the biological clock and affects the mammary glands

The jet lag paradigm disrupts circadian rhythms (*24*). Mice were exposed to an 8 h light advance repeated every 2–3 days (Fig. 1A). This jet lag paradigm mimics the CRD that humans face during shift work (*24*) or travel across time zones and increases tumor development in lung (*6, 7*), and breast (*9*). Female Friend LeukemiaVirus B (FVB) mice (4 weeks old) were housed under normal light and dark (LD 12:12), chronic jet lag, or chronic CRD conditions for 8 weeks before the mammary glands were collected every 4 h for 24 h. We confirmed that this jet-lag protocol disrupted circadian activity in our mouse model by assessing the locomotor activity (Fig. 1B). CRD did not significantly impact the weight of mice (Fig. S1A) ($P = 0.428$). Real-time PCR analysis showed that CRD affected the expression of core clock genes in the mammary glands, with a loss of periodic expression (PJTKcycle < 0.05) for most genes, including *Cry1*, *Cry2*, *Bmal1*, *Clock,* and *Per1* (Fig. 1C). *Per2* expression remained rhythmic in mice exposed to CRD (Fig. 1C), suggesting the desynchronization of the core clock components. To understand the effect of CRD on the mammary glands, we examined whole-mount preparations of inguinal mammary glands from LD and CRD mice at 12 weeks. Chronic CRD decreased branching (bifurcations) (Fig. 1D, upper panel, 1E, S1B) and the number of terminal end buds (TEBs) (Fig. 1D, lower panel, 1F, S1B) in the mammary glands of the studied mice. Compared with the mammary glands of LD mice (control), those of CRD mice showed a high frequency of ductal hyperplasia as found by using hematoxylin and eosin (H&E) (Fig. 1G) and by using Ki67 (Fig. 1H, S1C) of the mammary glands.

Chronic CRD accelerates aggressive mammary tumorigenesis and lung metastasis

To investigate the effect of circadian disruption on aggressive basal or triple-negative mammary tumorigenesis, we used preclinical GEMM of human basal tumors (FVB-Tg(C3-1-Tag)cJeg/JegJ (C3-Tag) (Jackson Labs strain 013591) (*25, 26*) that provides a model for examining how environmental factors impact aggressive mammary tumorigenesis and metastasis. Female hemizygous mice develop mammary gland adenocarcinomas at approximately 24 weeks of age for basal breast cancer or TNBC (*25, 26*). To investigate the effect of circadian disruption on tumorigenesis, mice were placed under LD or CRD conditions when they were 8 weeks old and maintained under CRD conditions through the end of the study at 27 weeks (Fig. 2A). The growth of primary tumors was measured every 3 days throughout this period. Because of the highly aggressive tumors in CRD mice, we euthanized the animals at 27 weeks. All mice were euthanized, and the tumor tissues were processed for other analyses. CRD did not significantly impact the weight of mice (Fig. S2A) ($P = 0.122$). Peripheral blood cell counts showed no significant

differences between CRD and LD mice (Fig. S2B, S2C). No significant changes were noted in the blood glucose (Fig. S2D), cholesterol (Fig. S2E), or amylase (Fig. S2F) levels in CRD mice, although the albumin-to-globulin ratio (AGR) was decreased (Fig. S2G). A high AGR shows a good prognosis for survival in different solid-tumor patients (*27*). CRD negatively affects cancer prognosis by decreasing the AGR. Single-cell RNA-sequencing (scRNA-seq; Fig. S3A) and real-time PCR (Fig. S3B) of tumor samples showed that CRD did not substantially alter the expression of Per genes (*Per1*, P = 0.141, and *Per2*, P = 0.88) (Fig. S3A, B) or other clock genes (*Clock*, P = 0.242, *Cry2*, P = 0.109) (Fig. S3A, B). *Cry1* expression significantly increased (P = 0.035) in CRD-induced tumors (Fig. S3B).

Animals placed in CRD conditions had a substantially increased mammary tumor burden (Fig. 2B) compared to the LD animals. CRD also accelerated tumor initiation at 18 weeks. In contrast, the average time of the tumor initiation for LD mice was 22 weeks (Fig. 2C). However, no difference was observed in the spectrum of tumor grades assessed using histopathology(*28*) between the two groups, with most tumors being grade 2 (Fig. S4A, B). Several technical differences, such as in the mouse genetic background (MMTV:PyMT C57BL/6J versus FVB-Tg(C3-1-TAg)cJeg/JegJ) and conditions of the animal facilities (such as light exposure) may explain why Hadadi *et al. (9)* observed an effect of CRD on tumor grade, but the same was not found in our study. The number of metastatic foci in the lungs was significantly higher (P =0.0002) in the CRD mice (Fig. 2D, E). To investigate the impact of CRD on tumor progression, 4T1 (mice triple-negative breast cancer cell line) cells were introduced into the female BALB/cJ mice via orthotopic transplantation into the 4th mammary glands. When mice developed palpable tumors (~4-5 days after injection), they were placed into LD or CRD conditions for 3 weeks until tumors became aggressive. CRD led to a modest but non-significant increase in tumor burden (Fig. S4C). This data suggests that CRD does not affect tumor progression events in this model. However, we did observe a significant increase in the formation of lung metastasis foci (Fig 2F, G). Flow cytometry was performed to investigate whether a higher metastatic potential was related to a higher cancer stem cell (CSC) population in CRD tumors. We observed a significant increase in the percentage of CSCs expressing CD49f markers (Fig. 2H, S4D) in CRD tumors compared with that in LD tumors. To investigate whether this enrichment was associated with an increase in the stemness potential of primary tumors, a mammosphere assay was performed using CRD and LD GEMM tumors. CRD tumor cells had a significantly higher (P<0.0001) mammosphere formation efficiency than LD tumor cells (Fig. 2I, S4E). Recent studies have used three-dimensional (3D) organoids as *in vitro* organs, with numerous applications ranging from disease modeling to drug screening (*29*). Using small intestinal crypt-derived organoids, a recent study showed that genetic disruption of the circadian clock accelerates intestinal organoid proliferation (*8*). We established 3D organoids (tumoroids) from LD and CRD tumors (Fig. 2J). Overall, CRD tumors exhibited more aggressive organoids than LD tumors.

Circadian desynchronization alters the TME

Breast TME is essential for the survival and immunosuppression of tumor cells (*30*). We performed scRNA analysis on cells isolated from GEMM basal tumor tissues. Our samples included two LD and two CRD types of breast tumors. Single cells were isolated from the tumors without surface marker selection. Using proper QC and filtration, we obtained single-cell transcriptomic data for the studied tumors (N= 2). To analyze different cell populations in the TME, 5,804 QC-positive single cells (LD and CRD tumors) were clustered according to their expression profiles (Fig. 3A), and 20,764 genes were identified. The Seurat package was used for preliminary clustering. Cells were clustered based on specific cell markers. Using the established expression markers, such as

for endothelial cells (*KLF2*)(*31*), M2 macrophages (*SLC2A1*)(*32*), TNBC cancer cells (*TRPS1*)(*33*), proliferating cells (*TOP2A)(34)*, myeloid cells (*FTH1)(35)*, progenitor cells (*NES*)(*36*), adipocytes (*CLEC11A*)(*37*), mesenchymal cells (*S100A4*)(*38*), angiogenic cells (*RPL35A*)(*39*), breast cancer stem cells *(FXYD3*)(*40*), dendritic cells (*CD68*) (*41*), cancer-associated fibroblast (*COL1A2*)(*42*), epithelial cells (*EPCAM*)(*43*), cycling cells (*CDK4*)(*44*), and B-cells (*CD83*) (*45*), we found that CRD altered different cell populations in the TME (Fig. 3B). This showed that CRD induced a higher number of M2-macrophage, TNBC cancer cells, cycling cells, adipocytes, cancer-associated fibroblasts (CAFs) and proliferating cells but a lower number of M1 macrophages, B-cells, and dendritic cells in the tumor (Fig. 3B). We next analyzed putative ligand–receptor (L-R) interactions in LD and CRD tumors and modeled cell–cell interactions between different cell types that play vital roles in maintaining cellular homeostasis. Cellular communication was investigated using CellChat, which shows the differences in the total number of L-R interactions between different cell types in LD vs CRD tumors (Fig. 3C). For example, the interaction between CAF with proliferating cells, TNBC cells, and M2 macrophages increased under CRD conditions compared to LD conditions (Fig. 3C). We identified 3429 and 3992 critical ligand-receptor pairings in LD and CRD tumors, respectively (Fig. S5A). Ligand–receptor interactions with increased and decreased strength were also identified (Fig. S5B). CellChat also identified signaling pathways linked to ligand-receptor interactions (Fig. 3D). Specific signaling pathways, including those involving fibroblast growth factor (FGF), WNT, and platelet-derived growth factor (PDGF), were exclusively detected in CRD tumors. Oncostatin M, Tumor necrosis factor (TNF), and NOTCH, were detected solely in LD tumors, and signaling pathways, including transforming growth factor β (TGFβ), epidermal growth factor (EGF), and fibronectin 1, were detected in both LD and CRD tumors (Fig. 3D). Gene Ontology (GO) analysis (Fig. 3E) indicated that genes associated with the acetyl CoA metabolic process, antigen processing (and presentation), nuclear division, regulation of cellular pH, carboxylic acid catabolic process, chromosome segregation were upregulated in CRD.

CRD induces immunosuppressive TME and turns tumors "cold"

The TME is critical for tumor progression and metastasis. Tumors are "hot" when they show signs of inflammation characterized by an infiltration of T cells mobilizing to fight the cancerous cells, whereas nonimmunogenic "cold" tumors lack infiltrating T cells, which makes it challenging to provoke an immune response with immunotherapy drugs (*46*). To investigate whether the increased prevalence of metastasis in CRD mice resulted from changes in the TME, we characterized different immune cell populations in the TME of LD and CRD tumors using scRNA-seq, flow cytometry, and multiplexing immunostaining (MxIF). We determined whether CRD could influence the proportion of various immune cells in the TME and, in turn, promote tumor progression and metastasis. scRNA-seq with GEMM tumors showed that CRD reduced cytotoxic T-cell infiltration (Fig. 4A) and enhanced regulatory T-cell (T_{reg}) infiltration (Fig. 4B). CRD induced M2 macrophage populations while decreasing M1 macrophage populations (Fig. 4C). There was an increase in $S100A4^+$ and α-smooth muscle actin (α-SMA^+) CAF populations in CRD-induced tumors compared to those in LD tumors (Fig. 4D). CRD increased EMT gene expressions, such as fibronectin 1 (*FN1*) and Snail (Snail 1) (Fig. 4E). Flow cytometry analysis with 4T1 tumors supported the scRNA seq data. FACS showed that CRD significantly enhanced the T_{reg} ($CD4^+FoxP3^+$) population (P=0.0359) (Fig. 4F). CRD induced M2 macrophage infiltration while reducing M1-macrophage infiltration (Fig. 4G). Tumors from mice under CRD conditions exhibited a ratio (M1:M2) that favored M2-mediated immunosuppression (Fig. 4H) and facilitated

tumor growth. CRD significantly enhanced $CD45^+$ immune cell population (P = 0.0029) in tumors (Fig. 4I). CRD reduced CD8 T-cells (cytotoxic T-cells) modestly but not significantly (P=0.66) (Fig. 4J). Our MxIF assay showed that CD8 T-cell infiltration was decreased, and FOXP3 (T_{reg}) expression was enhanced in CRD-induced GEMM tumors compared with those in LD GEMM tumors (Fig. 4K), making the tumor "cold." Our data suggest that CRD creates an immunosuppressive microenvironment by disrupting the immune system of the tumor. CRD enhances tumor progression and lung metastasis by enhancing the immunosuppressive microenvironment and increasing the CSC population. Our scRNA-seq, FACS, and MxIF results confirmed the "cold" characteristics of CRD tumors. The gating strategy used for flow cytometry is shown in Fig. S6. Chemokines play a pivotal role in the migration pattern of immune cells into the tumor and facilitate the immunosuppressive TME by enhancing the differentiation and infiltration of immunosuppressive pro-tumorigenic cells such as T_{reg} cells, myeloid-derived suppressor cells (MDSCs), and tumor-associated macrophages (TAMs). To investigate whether CRD altered the chemokine-cytokine network in the studied mice, we quantified the levels of 40 circulating chemokines in the plasma of LD and CRD mice using a Proteome Profiler. Marked increases in circulating IFN-γ, IL-1β, G-CSF, and IL-16 levels were observed in CRD mice (Fig. S7A). As plasma cytokine/chemokine levels do not represent the TME, we used the data from our scRNA-seq and real-time PCR to assess chemokine/cytokine network expression levels in LD and CRD tumors. Levels of specific cytokines/chemokines known to favor an immunosuppressive microenvironment (*47*), such as CCL12 (Fig. 4L) and CXCL5(Fig. 4M), were upregulated in CRD-induced GEMM tumors. Levels of CCL28, known to induce T_{reg} infiltration and create an immunosuppressive environment (*48*), were upregulated in CRD tumors, as shown using scRNA-seq (Fig. S7B), but not significantly, as shown using real-time PCR (Fig. S7C). Levels of IL-17β and IL10, were upregulated modestly (but not significantly) in CRD-induced 4T1 tumors (Fig. S7C).

Malignant human breast cancer cells have high CRD

Earlier studies (*9*) and the present study used GEMMs to investigate the effect of CRD on tumorigenesis. Several studies have identified key circadian genes. However, more insights are needed into the molecular mechanisms underlying CRD at the single-cell level and in human tumors. To investigate the process underlying CRD during mammary tumorigenesis, we used a scRNA sequence dataset from a previously published study (*49*). The dataset included TNBC, HER2-positive, and luminal tumors. Using large-scale copy number variation from the transcriptomics data (*50*), we separated definitive malignant cells from potential nonmalignant cell populations in TNBC (Fig. 5A), luminal (ER^+/PR^+) (Fig. S8A), and HER2 tumors (Fig. S8B). Based on a previous study (*51*), the CRD score was calculated using the expression of 358 circadian-related genes (*51*). Next, we quantified the CRD scores of malignant (and nonmalignant) cells in different types of human breast tumors. Aggressive TNBC comprised significantly ($P < 0.01$) more malignant cells with high CRD scores (Fig. 5B) than luminal tumors (Fig. S8C). Malignant cells in HER2 tumors also showed a high CRD score (Fig S8D). *Cry1*, *Per1*, and *Per2* expression decreased in TNBC malignant cells compared to non-malignant cells, as shown using the scRNA-seq dataset (Fig. 5C). To define the role of CRD in large patient populations, we used publicly available RNA-seq data from tumors (N=1104 patients) and surrounding tissues (N = 113) of patients with breast cancer in The Cancer Genome Atlas (TCGA). The expression of core clock genes (*Per1*, *Per2*, *Per3*, *Cry2*, *Rorc*, *Rorb*, *Nr1d1*, and *Arnt2*) was significantly ($P < 0.05$) lower in the tumors than in the surrounding tissues (Fig. 5D). These data suggest that the core clock is disrupted in human breast tumors.

CRD creates "cold" tumors by inducing LILRB4 expression

Next, to identify the molecular mechanism that regulates the CRD-induced immunosuppressive TME, we searched for transcripts differentially expressed between the samples (mammary tumors and glands) collected from mice exposed to ordinary light and dark conditions (LD 12:12) and mice subjected to CRD. Differential gene expression (DGE) analysis of our scRNA-seq data revealed that LILRB4 was upregulated in the tumor samples from CRD-induced GEMMs (Fig. 6A). LILRB4, an immunoreceptor tyrosine-based inhibitory motif-containing receptor, suppresses T-cell activity via a signaling pathway involving apolipoprotein E (APOE), SH2 domain-containing protein tyrosine phosphatase-2 (SHP-2), urokinase-like plasminogen activator (uPAR or Plaur), and arginase 1 (ARG-1) (*29*). Recent studies have shown that LILRB4 creates an immunosuppressive microenvironment in AML (*23*) and solid cancers (*22*) by inhibiting $CD8^+$ T-cell infiltration and inducing T_{reg}. Real-time PCR showed that CRD enhanced LILRB4 transcript levels significantly in the CRD-induced GEMM tumors (P=0.033) (Fig. 6B), and CRD-induced 4T1 tumors (P=0.024) (Fig. 6C). The immunofluorescence analysis showed an elevation of ARG1 expression in CRD-induced GEMM tumors (Fig. 6D). The transcript level of ARG1 was significantly (P = 0.047) increased in CRD-induced tumors (Fig. 6E). Increased LILRB4 expression enhanced the immunosuppressive TME as CD8 infiltration decreased, whereas M2 macrophage (CD163) and T_{reg} (FOXP3) populations increased in CRD-induced mammary tumors from GEMMs, as shown using multiplex immunofluorescence histochemistry (mIHC) (Fig. 6F). Furthermore, LILRB4 transcript levels were significantly increased (P=0.026) in CRD-induced mammary glands (Fig. 6G). Mammary gland LILRB4 transcript levels exhibited robust diurnal oscillations, increasing during the light phase under normal and dark conditions. Under CRD, the amplitude of this rhythm was dampened, but the phase was reserved (or only slightly shifted), and the transcript level peaked during the dark phase (Fig. S9B). The transcript level of ARG1 increased modestly but non-significantly (P=0.061) in the CRD-induced mammary glands (Fig. S9C). The transcript level of the chemokine CCL12 increased significantly (P=0.0067) in CRD-induced mammary glands (Fig. S9D). The transcript level of CXCL5 is raised modestly but not significantly (P=0.27) in CRD-induced mammary glands (Fig. S9E). Overall, these changes in the immune milieus of the CRD-induced mammary microenvironment can decrease adaptive immunity and enhance susceptibility to cancer and other diseases.

Discussion

Previous studies have shown an association between CRD and an increased risk of cancer (*6-8, 12*). Following the chronic jet lag protocol, here, we showed that CRD interrupted the biological clock and affected the mammary gland morphology. Chronic CRD accelerated aggressive mammary tumorigenesis and lung metastasis by altering the TME. CRD induced an immunosuppressive TME and turned tumors "cold." Malignant human breast cancer cells had high CRD scores. We also identified the molecular mechanisms underlying CRD-induced aggressive mammary tumorigenesis: CRD created "cold" tumors by inducing LILRB4 expression.

We found that CRD alters mammary gland morphology. The CRD-induced mammary glands exhibited underdeveloped terminal end buds (TEBs) and reduced branching morphology. CRD-induced mice showed mammary gland ductal hyperplasia, which can be the early sign of ductal cancer (*52*), as seen by H&E and Ki67 staining. This indicates the role of the circadian clock in mammary gland development and the potential role of CRD in breast cancer. Our study showed that CRD accelerated spontaneous mammary tumorigenesis and lung metastasis but not tumor progression, indicating that CRD affects the early events of tumor initiation rather than the growth

of the established tumors. LILRB4 expression was increased in mammary glands and CRD-induced mammary tumors, revealing an unidentified mechanism responsible for CRD-induced tumorigenesis, lung metastasis, and mammary gland development. The jet lag protocol used here mimics the effects of rotating shift work or frequent eastbound trans-meridian flights and has been previously shown to cause severe perturbations of circadian rhythmicity (*6, 7, 9*). A recent epidemiological study showed that night shift work affects the risk of developing breast cancer by 2.34 times (*53*). Consistent with the results of published studies (*7*), we found that CRD affected the rhythmicity of many clock genes (e.g., *Clock, Bmal1, Per1*, and *Cry1*) in the mammary glands; however, *Per2* expression remained rhythmic after CRD, indicating that *Per2* is more sensitive to phase entrainment signals of molecular oscillators in peripheral tissues.

Using scRNA-seq and TCGA data, we showed that the expression of certain circadian genes was decreased in aggressive human TNBCs compared with that in the surrounding mammary tissues. Our analysis also showed that in aggressive human TNBCs, malignant cells had higher CRD scores than nonmalignant cells. *PER1*, *PER2*, and *CRY1* expression were significantly lower in malignant cells than in nonmalignant TNBC cells. Gene expression analysis using TCGA data showed that the expression of several clock genes (*PER1*, *PER2*, *PER3*, *CRY2*, *ARNT2*, *NR1D1*, *RORB*, and *RORC*) differed substantially between the tumor and normal surrounding tissues. Therefore, it is important to investigate the rhythmic pattern of the clock genes inside the tumors. Our findings also indicated that CRD induced tumor immune microenvironment remodeling, desynchronized the immune response, and enhanced the immunosuppressive TME, which could be involved in increased tumor burden in mice maintained under the CRD schedule. The TME consists of natural killer cells, $CD8^+$ T cells, $CD4^+$ helper T (T_h) cells, proinflammatory macrophages (M1), and dendritic cells, which elicit antitumor immune responses, whereas the presence of MDSCs and $FOXP3^+$ T_{reg} counteracts tumor immunity (*54*). Tumor cells escape immune cells through several mechanisms, including releasing immunosuppressive cytokines/chemokines (such as transforming growth factor β and interleukins or ILs). Tumor-released molecules shape the TME and induce immunosuppression, which decreases antitumor immune responses. CRD alters tumor immunity by modulating the cytokine-chemokine network (*9*). Our scRNA-seq and real-time PCR studies showed that CRD induced a pro-tumorigenic and immunosuppressive microenvironment by increasing the expression of CCL12 and CXCL5. The upregulation of CCL12 (human orthologs of CCL2) (*55*) and CXCL5 reportedly leads to the accumulation of MDSCs (*56*). MDSCs create an immunosuppressive environment by suppressing T-cell responses and $CD8^+$ T-cell infiltration (*56*). CRD also enhances CCL28 production, which leads to the recruitment of T_{reg} cells in the TME (*57*).

Our scRNA-seq study showed that CRD altered various cell populations in the TME. CRD decreased cytotoxic T-cell infiltration and the dendritic cell population and increased the T_{reg} cell population, which induces an immunosuppressive microenvironment. This supports the recent finding that dendritic cell- and T-cell-autonomous circadian clocks are responsible for time-of-the-day-dependent antitumor effects (*58*). CRD-induced $S100a4^+$ CAF, and α-SMA^+ CAF populations are known to promote tumor progression and metastasis and contribute to an immunosuppressive TME (*59*). In line with the results of a previous study (*60*), we found an increase in the M2 macrophage population and a decrease in the M1 macrophage population in CRD tumors. M2 macrophages play a significant role in creating an immunosuppressive microenvironment (*61*), whereas M1 macrophages induce inflammation and kill tumor cells (*61, 62*). Our FACS results corroborated the scRNA-seq results and further confirmed that CRD decreased cytotoxic T-cell

infiltration and enhanced the T_{reg} population. CRD increased the leukocyte ($CD45^+$) population, corroborating that the jet lag schedule enhances leukocyte levels in melanoma (*60*).

In this study, we further demonstrated that CRD enhanced the expression of LILRB4 *in vivo* in healthy mammary glands and mammary tumors. LILRB4 is an inhibitory receptor that plays a key role in immune checkpoint pathways (*63*). Regarding signals transmitted by LILRs, the cytoplasmic immunoreceptor tyrosine-based inhibitory motifs (ITIMs) and immunoreceptor tyrosine-based activating motifs (ITAMs) are of great significance (*64*). The soluble form of LILRB4 (also known as LILR-Fcs) can effectively inhibit T-cell proliferation, even in the absence of antigen-presenting cells (APCs) (*65*). LILRB4 inhibited the differentiation of $CD8^+$ and $CD4^+$ T cells (*23*). By activating the JAK/STAT signaling pathway, LILRB4 controls the expression of cytokines in macrophages (*66*). In tumors, LILRB4 binds to the ligand CD166 (an activated leukocyte adhesion molecule) to inhibit $CD4^+$ Th-cell proliferation and promote tumor growth and infiltration (*67*). In different malignant cancers, LILRB4 expression in MDSCs is associated with decreased survival in patients (*68*). Multiple studies have shown that LILRB4 expression is higher in AML and negatively correlated with the overall survival of AML patients (*23, 69*). Another study showed that APOE binds to AML cells infiltrating the tissue through LILRB4, causing T-cell suppression and tumor infiltration (*23*). LILRB4 organizes tumor invasion pathways in AML by creating an immunosuppressive microenvironment (*23*). LILRB4 suppresses T-cell activity via a signaling pathway involving APOE, SHP-2, uPAR, and ARG1 in AML (*23*). A recent study showed that LILRB4 blockade increased the proportions of tumor immune infiltrates, effector (T_{eff}) levels, and altered the TME toward reduced immunosuppression in solid tumors (*22*). In addition, LILRB4 reduces the expression of inflammatory chemokines/cytokines (*70*) and increases the expression of immunosuppressive cytokines, such as CCL12 and CXCL5. Together, these findings reveal that LILRB4 creates an immunosuppressive microenvironment, thereby decreasing its antitumor efficacy. LILRB4 expression is upregulated under pathological conditions, such as Kawasaki disease, systemic lupus erythematosus, sepsis, and mental illness, in addition to tumors (*71*). CRD alters several cell-autonomous mechanisms to induce tumorigenesis. Our study showed that CRD activated LILRB4 signaling in healthy mammary glands and aggressive TNBCs. Using real-time PCR and immunofluorescence analysis, we observed increased *ARG1* expression (LILRB4 target gene) in CRD-induced tumors. Analysis of the TME using multiplexing immunostaining showed an immunosuppressive microenvironment as the cytotoxic T-cell and M1 macrophage populations decreased. In contrast, T_{reg}, and M2 macrophage populations were increased in CRD tumors. We found that the disruption of circadian rhythm upregulated LILRB4 expression, which correlated with mammary tumor progression and abnormal morphology in the mammary glands.

CRD upregulated the expression of immunosuppressive chemokines (CCL12) in mouse mammary glands. CCL2 (an orthologous of mouse CCL12) increases stromal density and elevates cancer risk (*72*). An immunosuppressive environment can increase susceptibility to opportunistic infections (*73*) in CRD-induced patients. This study demonstrated how an inhibitory immune receptor altered the TME and influenced aggressive mammary tumorigenesis in response to CRD. LILRB4 expression, in response to CRD, may play an essential role in tumorigenesis by creating an immunosuppressive microenvironment.

Our data confirmed the expression of LILRB4 target genes in CRD tumors and mammary glands. Our findings suggest that LILRB4 is a potential therapeutic target for mitigating CRD-induced cancer risk in populations exposed to chronic CRD, such as shift workers. LILRB4 inhibition was also found to improve the immunosuppressive microenvironment. However, how

the disruption of the cell-autonomous molecular clock by CRD could enhance LILRB4 expression remains unknown. Further investigations are needed to determine why and how CRD enhances LILRB4 expression. *In vitro* and *in vivo* systems of tumor cell-specific deletion of core clock components will be needed to understand the cell-autonomous circadian control that ignites mammary tumorigenesis. Additional investigations are needed to determine whether the chronic elevation of LILRB4 levels in the mammary glands in response to CRD occurs early in the disease process and whether LILRB4 is present in other anatomical locations.

In conclusion, our study provides experimental evidence of the link between CRD and aggressive triple-negative mammary tumorigenesis, metastasis, and abnormal mammary gland morphology. By upregulating LILRB4 expression, CRD creates an immunosuppressive microenvironment by reducing antitumor immunity, altering the cytokine/chemokine network, and creating a pro-tumorigenic microenvironment. Based on our data, we propose a signaling cascade (Fig. **7)** as a possible mechanism behind CRD-induced mammary gland disruption, enhanced aggressive tumorigenesis, lung metastasis, and immunosuppressive TME. Finally, our findings showed that CRD induces an immunosuppressive mammary microenvironment that promotes cancer progression. Clock disruption is experienced by many individuals annually, and its effects are associated with many adverse health effects, as mentioned earlier. In addition to jet lag and shift work, numerous other factors lead to CRD, including metabolic stress (induced by starvation and high-calorie diets), metabolic disorders, aging, stress, and social behaviors. Whether the effects observed here can be generalized to other environmental factors that influence the circadian clock remains to be determined.

Materials and Methods

A. Animal husbandry:

Nulliparous female mice were purchased from Jackson Laboratory. The mice were housed under 12 h light and 12 h dark (LD 12:12) and circadian rhythm disruption (CRD) conditions at room temperature (25°C), and food and water were provided *ad libitum*. Four-week-old genetically engineered mice (GEM), i.e., FVB-Tg(C3-1-Tag)cJeg/JegJ mice (Jax stock #013591), were caged until they were 27 weeks old. Under identical light conditions, normal FVB mice (Jax stock #001800) were used for the experiments involving mouse mammary glands and were housed for eight weeks before they were sacrificed. BALB/cJ mice (Jax stock #000651) were used to introduce mouse cancer cell lines (4T1) and were housed under LD 12:12 or CRD conditions. All animal care and treatments were per the Institutional Animal Care and Use Committee of Texas A&M University under protocol # 2022-0094.

B. CRD conditions:

Mice were grouped randomly for exposure to standard light conditions (LD 12:12) or CRD light conditions (consisting of an 8-hour light phase advance repeated every two days) (*6, 7, 74*). FVB-Tg(C3-1-Tag)cJeg/JegJ mice were kept under normal (LD) conditions until 8 weeks of age. At 8 weeks, they were randomly assigned either to remain in LD or to be exposed to CRD or jet-lag (JL) conditions, with an 8-hour advance in the light/dark cycle every 2 days. All mice had free access to food and water. Zeitgeber time (ZT) 0 corresponded to the onset of light, while ZT12 corresponded to the onset of dark.

C. Running wheel activity analysis:

The LD 12:12 and CRD animal groups were provided access to running wheels (Columbus Instruments) with unrestrained access to standard mouse chow and drinking water for several weeks. ActogramJ (ImageJ) was used to assess voluntary running activities in the form of electronically stored records of the wheel rotation (*75*).

D. 4T1 cell mouse TNBC model:

The mouse TNBC model was prepared with minor modifications to the standard protocol (*76*). 4T1 cell lines were obtained from the American Type Culture Collection (ATCC, CRL-2539™) and cultured and maintained in RPMI-1640 (ATCC, 30-2001) with high glucose, L-Glutamine, and HEPES (4-(2-hydroxyethyl)-1-piperazineethanesulfonic acid) buffer system, under 5% CO2 atmosphere at 37°C. The cell culture medium was supplemented with 10% fetal bovine serum (FBS) (Sigma-Aldrich, F2442) and 1% penicillin and streptomycin (Sigma Aldrich, P4333). In each mouse, 10,000 cells suspended in sterile PBS were injected subcutaneously into the 4th mammary gland fat pad. The mice were housed in LD or CRD conditions for 3-4 weeks before they were sacrificed to harvest the tumors.

E. Histology and tumor burden analysis:

Following the development and maintenance under the aforementioned chronic conditions, the tumors and the mammary glands were harvested using aseptic techniques. Tumor volumes were calculated for each breast tumor using caliper measurements after every 3 days. $Tumor\ volume\ = (length\ \times width\text{^}2\ )/2$ was used to measure the volume of the tumors (*77*), whereas the equation $Tumor\ burden\ (in\ percentage)\ = (Tumor\ weight\ /mice\ body\ weight) \times 100\ \%$ was considered to determine the tumor burden (*9*). Following the sacrifice of the animals by cervical dislocation, the tumor, or the lung samples were fixed in 10% neutral buffered formalin (NBF) for 48 hours before being transferred to the Research Histology Unit of the VMBS Core Histology lab at Texas A&M University for subsequent paraffin embedding and sectioning at a thickness of 4 µm. The tissue sections were stained with hematoxylin and eosin (H&E) for pathological examinations.

F. Immunohistochemistry:

The formalin-fixed paraffin-embedded (FFPE) mouse mammary gland tissues on glass slides were deparaffinized by incubating at 65°C for 2 hours, followed by dipping in xylene for 5 minutes each time for two changes. IHC kit manufacturer's protocol (Abcam, ab64264) was followed to inhibit any endogenous peroxidase activity by treating the tissue with hydrogen peroxide. Antigen retrieval was carried out by incubating the slides in pre-heated citrate antigen retrieval buffer (10 mM citrate, 0.05% Tween 20, pH 6.0) at 95°C for 20-25 minutes in a water bath. After blocking, the tissues were incubated overnight at 4°C with anti-ki67 polyclonal antibody (ABclonal, A16919), dissolved in the kit blocking solution. Following incubation with the secondary antibody availed with the IHC kit, the expression was visualized with DAB peroxidase substrate (Abcam, ab64264). The slides were counterstained with Mayer's Hematoxylin Solution (VitroVivo Biotech, VB-3000-1) for 2 minutes and blued under running tap water for 5 minutes before being mounted with Optic Mount I™ xylene mounting medium (Mercedes Scientific). The immunostained mouse mammary glands were imaged with the Echo Revolve R4 fluorescent microscope

(Echo). Quantitation of the ki67-positive nuclei was performed manually and plotted using Prism8 (GraphPad Inc.).

G. Whole mount staining of mouse mammary gland:

The mammary gland tissues were spread on glass slides immediately after harvesting and kept for drying for 5 minutes to get the tissue stuck to the glass slides. The mammary glands were then fixed using Carnoy's fixative solution (VitroVivo Biotech, VB-3001-1) for three hours, followed by washing in 70% ethanol for 30 minutes. Following gradual stepwise hydration and rinsing in distilled water, the tissues were incubated overnight at room temperature (RT) with Carmine Alum Staining Solution (VitroVivo Biotech, VB-3001-2). Stained tissues were dehydrated with gradients of ethanol concentrations and finally with three changes of xylene bath of 10 minutes each. The slides were then mounted with Optic Mount I™ xylene mounting medium (Mercedes Scientific) and observed under the microscope (Echo).

H. Single-cell RNA sequencing (scRNA Seq):

The tumors were maintained under sterile conditions during the harvesting step. After brief washing in chilled sterile PBS, the tumors were kept in Dulbecco's Modified Eagle Medium (DMEM) (ATCC, 30-2002), supplemented with 10% FBS (Sigma-Aldrich, F2442) and 1% antibiotic solution (Sigma Aldrich, P4333) on ice until minced and subsequently blended with gentleMACS Dissociator (Miltenyi Biotec, 130-093-235). MACS Miltenyi Tumor Dissociation Kit for mice (Miltenyi Biotech, 130-096-730) was used for further enzymatic digestion according to the manufacturer's protocol for preparing the single-cell suspension. The cells were then rinsed with complete DMEM cell culture medium and filtered with 70 µm sterile MACS® SmartStrainers (Miltenyi Biotec, 130-098-462). The single-cell suspension was treated for 5 minutes in red blood cell lysis buffer before being resuspended in 0.04% BSA in 1x DPBS solution. The suspension of cells was then transferred to the Texas A&M Institute for Genome Sciences and Society (TIGSS) for scRNA-seq. Single-cell sequencing libraries were prepared on the Chromium platform (10x Genomics) using the Single Cell 5' v2 Full Kit (PN-1000263). Libraries were sequenced at the North Texas Genome Center, on the NovaSeq6000 sequencer (Illumina). Raw intensity files from the sequencing run were demultiplexed and base called using CellRanger (10x Genomics) mkfastq. Demultiplexed fastq files were mapped to the mouse reference (mm10, GCF_000001635.20) transcriptome and counted using CellRanger count. Filtering and processing the count matrixes output from CellRanger were completed in the Seurat v5 toolkit. Samples were then integrated into a single Seurat object. Non-single cell captures from the 10x Genomics capture platform were filtered by removing cells with greater than 7,500 and less than 200 mRNA features. Apoptotic cells were filtered by removing any cells that expressed greater than 10% mitochondrial genes of the total gene expression profile. The integrated data was scaled, neighbors calculated using a KNN method, and clustering was performed using the Louvian algorithm. Non-linear dimensional reduction was performed using UMAP. Cell type assignment was performed manually based on unique marker genes identified in each cell cluster from the UMAP reduction. Markers were cross-referenced with published literature specific to mouse mammary gland tissues. Differentially expressed genes were identified using the MAST (*78*) R package, and GO pathway enrichment analysis was performed with the clusterProfiler (*79*) R package.

Cellular communication analysis: The CellChat R package analyzed cellular communication using default parameters. Each sample was analyzed separately and then

merged into a single CellChat object. The total number of interactions and strengths were computed using the "compareInteractions" function. The most significant pathways were identified using the "rankNet" function and visualized with the "netVisual_diffInteraction" function.

I. *In vitro* tumorosphere formation assay:

The dissociated single cells from the GEMM animal models were cultured in ultra-low attachment 96-well plates (ThermoFisher Scientific, 174927) in EpiCult™-B (mouse) medium supplemented with human recombinant EGF (hrEGF) (Stem Cell Technologies, 78006), human recombinant bFGF (hrbFGF) (Stem Cell Technologies, 78003), and heparin (Stem Cell Technologies, 07980). 500 cells per well from LD 12:12 and CRD group tumors were added and incubated with standard cell culture conditions for 5 days in the CO_2 incubator before being observed under the microscope. The number and the size of the tumorospheres were observed and compared between LD and CRD tumors.

J. Organoid assay:

Singlet cells from tumors of both conditions (LD and CRD) were re-suspended in Geltrex™ (Gibco, ThermoFisher, A1413202) and plated on a 24-well plate. After the gel was solidified to form the matrix, EpiCult™-B (mouse) medium supplemented with hrEGF, hrbFGF, and heparin was added to assess the growth of the mouse mammary tumor cells from LD 12:12 and CRD conditions. After 7 days of incubation, the organoids formed were imaged under the microscope. The culture medium was changed after every two days.

K. Flow cytometry:

The tumors from GEMM and BALB/cJ mice were dissociated using the similar protocol mentioned in single-cell isolation (H), and the cells were counted and resuspended in 1 ml of cell staining buffer (CSB) (BioLegend, 420201) for each sample. Zombie NIR™ Fixable Viability Kit (BioLegend, 423105) was diluted in CSB and applied to cells on ice for 20 min in the dark on ice. After washing with CSB, cells were spun down at 400 x g for 4 minutes and resuspended in 50 µl of the CSB before being incubated with fluorochrome-conjugated antibodies (Alexa Fluor® 700 anti-mouse CD4, Pacific Blue™ anti-mouse CD8a, Alexa Fluor® 488 anti-mouse CD86, PE anti-mouse CD163, Alexa Fluor® 594 anti-mouse CD45) in the dark for 20 minutes following the recommended dilutions. Cells were fixed and permeabilized using 2% paraformaldehyde and 0.1% Triton X-100 in PBS, respectively, and stained with FoxP3 (Alexa Fluor® 488 anti-mouse/rat/human FOXP3) for 20 minutes in the dark at 4°C. Afterward, stained cells were rinsed with PBS and kept in PBS at 4°C in the dark until analyzed. Cytek Aurora spectral flow cytometer was used for the analysis and was carried out at TAMU Flow Cytometry Facility.

L. Quantitative PCR for detecting mRNA levels:

Following harvesting of the mammary glands and the tumors, total RNA was extracted using Quick-RNA™ MiniPrep (Zymo Research, R1054), and the purity was analyzed by DeNovix DS-11 Series nanodrop Spectrophotometer (DeNovix). 1 µg of total RNA from each sample was reverse transcribed to cDNA by High-Capacity cDNA Reverse Transcription Kit (Applied Biosystems™, 4368814). Analysis for gene expression by quantitative real-time PCR was performed using SsoAdvanced Universal SYBR Green Supermix (BioRad, 1725271).

M. Human CRD analysis for breast cancer patients:

All statistical analyses were performed using the R software package (version 4.3.0.). scRNA-seq data corresponding to the triple-negative breast cancer (TNBC) patients from

Wu *et al.*, 2021 (*49*) were pre-processed using standard steps outlined in Hao *et al.,* (*80*). In particular, the features (genes) detected in at least 3 cells and cells showing expression of at least 200 features were considered for downstream analysis. The data were log-normalized by library size and multiplied by a scale factor 10,000. The data were further scaled such that the mean expression across cells is 0 and the variance across cells is 1. The uniform manifold approximation and projection (UMAP) was performed on the processed data. The UMAP plot with cells clustered according to the inferCNV cell type. The cells which had no infer-CNV call are denoted as "unknown." To investigate the level of circadian rhythm disruption in each cell, we calculated the CRD scores for the 358 circadian-related genes (CRGs) following He *et al.,* 2022 (*51*) separately for malignant and non-malignant cells. A cutoff of 75% based on quartiles was used as the threshold for the CRD level to segregate the scores as high (denoted as CRD^{hi}) and low (denoted as CRD^{low}). The percentage of cells that show CRD^{hi} scores by cell type, along with the p-value of the corresponding Binomial proportion test, is used for this study. The mean normalized expression of the core circadian genes by the cell type (malignant and non-malignant) is presented in this study. A gene-wise paired t-test was conducted to test for the difference in their mean expression between malignant and non-malignant cells. The genes that show a significant difference in expression are shown in "red", while the insignificant ones are shown in "black". Bulk RNA-sequencing data from the publicly available TCGA BRCA dataset was used further to explore the expression pattern of the core circadian genes. The patients were segregated according to the analyzed tissue type, i.e., "Tumor" and "Surrounding" tissue. The mean expression of the genes (+/- standard error of mean) over patients by the type of tissue analyzed. The Wilcoxon signed-rank test was used to test for the difference in expression between the tumor and surrounding tissues for each gene. The genes showing a significant difference are labelled in "red", while the insignificant genes are marked in "black".

N. Blood chemistry and cytokine array:
Pre-mortem terminal blood was collected from the FVB-Tg(C3-1-Tag)cJeg/JegJ mice. The blood samples were transferred to the Texas A&M Veterinary Medical Diagnostic Laboratory (TVMDL) to analyze the blood chemistry parameters. The cytokine array was performed using the Proteome Profiler Mouse XL Cytokine Array kit (R&D Systems, ARY028). The blood samples were kept undisturbed for 30 minutes at room temperature before being spun at 2000 x g for 10 minutes at 4°C. Then, the serum was separated for the cytokine array profiling according to the manufacturer's protocol. Afterward, the array membranes were scanned using ChemiDoc Imaging System (BioRad, 12003153). ImageJ was used to quantitate the dots on the array membrane. Data were plotted using Prism8 (GraphPad, Inc.).

O. mIF Staining of Mouse Tissues: The panels were developed and optimized for use in mouse tissue. The following primary antibodies from Fortis Life Sciences, Cell Signaling Technology, and ABclonal were utilized for both immunohistochemical and immunofluorescence staining: rabbit anti-mouse ARG1 [BLR161J], rabbit anti-human/mouse LILRB4 [A7073], rabbit anti-human/mouse CD163 [BLR087G], rabbit anti-mouse CD8a [BLR173J], and rabbit anti-mouse FOXP3 [D6O8R], and rabbit anti-mouse CD4 [BLR167J]. Antibody concentration and staining order were optimized using FFPE mouse immune tissue microarray serial sections. Each target was evaluated for overall signal: noise ratio, loss of signal intensity, and overall autofluorescence in the first,

third, or sixth positions via heat-induced epitope retrieval (HIER) methods. The final optimized order was then subjected to the Opal method of multiplex immunofluorescence (see below). Multiplex immunofluorescence staining was performed with the Akoya Opal™ Polaris 7-color IHC kit fluorophores (Akoya Biosciences [NEL861001KT]). FFPE tissue sections were baked for 30 minutes, deparaffinized in xylene, and rehydrated by serial passage through graded concentrations of ethanol. Endogenous peroxidase in tissues was blocked with 0.9% H_2O_2/methanol for 40 min. Multiple (7) sequential HIER treatments were performed for 20 min each at 92-96°C in Citrate pH 6.0 (first cycle) or Tris EDTA pH9 (remaining cycles) buffer. After each HIER cycle, sections were rinsed with DI water and cooled at RT for 20 minutes. Tissue sections were circled with hydrophobic barrier pens and blocked with 20% normal goat serum for 20 minutes before incubation with primary antibody for 20 min. Then, sections were rinsed with TBST for 10 min and incubated with HRP-conjugated secondary (A120-501P) for 20 min, followed by another 10 min rinse in TBST. Incubation with an Opal fluorophore (Opal480, Opal520, Opal570, Opal620, Opal690) was then done for 10 min, followed by a 10 min rinse in DI water. Bound primary and secondary antibodies were then subject to the next HIER treatment (as aforementioned) for 20 min. After washing in DI water and cooling at RT for 20 min, the process of staining and antibody removal was repeated for the desired number of targets. Finally, after staining with the sixth Opal fluorophore (TSA-DIG), an additional HIER cycle (7th) was performed. Finally, the tissue specimens were stained with 4′,6-diamidino-2-phenylindole (DAPI) for 10 min and mounted in VECTASHIELD Vibrance Antifade Mounting Medium (ThermoFisher Scientific). Akoya Biosciences' PhenoImager HT (formerly known as Vectra Polaris Automated Quantitative Pathology Imaging System) was used for multispectral imaging at 40× magnification.

P. Statistical analysis:

GraphPad Prism8 was used as the Statistical analysis tool except for the assessment of the rhythmicity that was carried out using the JTK cycle. The significance was assessed using either an Unpaired t-test or analysis of variance (ANOVA), with a false positive threshold of 0.05 considered acceptable ($p<0.05$). Unless otherwise mentioned, the data were presented as mean ± standard error of the mean (SEM).

Reference:

1. F. C. Kelleher, A. Rao, A. Maguire, Circadian molecular clocks and cancer. *Cancer Lett* **342**, 9-18 (2014).
2. S. Panda, M. P. Antoch, B. H. Miller, A. I. Su, A. B. Schook, M. Straume, P. G. Schultz, S. A. Kay, J. S. Takahashi, J. B. Hogenesch, Coordinated transcription of key pathways in the mouse by the circadian clock. *Cell* **109**, 307-320 (2002).
3. K. F. Storch, O. Lipan, I. Leykin, N. Viswanathan, F. C. Davis, W. H. Wong, C. J. Weitz, Extensive and divergent circadian gene expression in liver and heart. *Nature* **417**, 78-83 (2002).
4. A. Hemmer, J. Mareschal, C. Dibner, J. A. Pralong, V. Dorribo, S. Perrig, L. Genton, C. Pichard, T. H. Collet, The Effects of Shift Work on Cardio-Metabolic Diseases and Eating Patterns. *Nutrients* **13**, (2021).
5. https://wwwn.cdc.gov/Niosh-whc/chart/OHS-WORKORG?OU=*&T=OU&V=R.
6. T. Papagiannakopoulos, Matthew R. Bauer, Shawn M. Davidson, M. Heimann, L. Subbaraj, A. Bhutkar, J. Bartlebaugh, Matthew G. Vander Heiden, T. Jacks, Circadian Rhythm Disruption Promotes Lung Tumorigenesis. *Cell Metabolism* **24**, 324-331 (2016).
7. M. Pariollaud, L. H. Ibrahim, E. Irizarry, R. M. Mello, A. B. Chan, B. J. Altman, R. J. Shaw, M. J. Bollong, R. L. Wiseman, K. A. Lamia, Circadian disruption enhances HSF1 signaling and tumorigenesis in Kras-driven lung cancer. *Science Advances* **8**, eabo1123 (2022).
8. S. K. Chun, B. M. Fortin, R. C. Fellows, A. N. Habowski, A. Verlande, W. A. Song, A. L. Mahieu, A. E. Y. T. Lefebvre, J. N. Sterrenberg, L. M. Velez, M. A. Digman, R. A. Edwards, N. R. Pannunzio, M. M. Seldin, M. L. Waterman, S. Masri, Disruption of the circadian clock drives Apc loss of heterozygosity to accelerate colorectal cancer. *Science advances* **8**, eabo2389 (2022).
9. E. Hadadi, W. Taylor, X.-M. Li, Y. Aslan, M. Villote, J. Rivière, G. Duvallet, C. Auriau, S. Dulong, I. Raymond-Letron, S. Provot, A. Bennaceur-Griscelli, H. Acloque, Chronic circadian disruption modulates breast cancer stemness and immune microenvironment to drive metastasis in mice. *Nature Communications* **11**, 3193 (2020).
10. K. C. G. Van Dycke, W. Rodenburg, C. T. M. van Oostrom, L. W. M. van Kerkhof, J. L. A. Pennings, T. Roenneberg, H. van Steeg, G. T. J. van der Horst, Chronically Alternating Light Cycles Increase Breast Cancer Risk in Mice. *Curr Biol* **25**, 1932-1937 (2015).
11. V. Blakeman, J. L. Williams, Q. J. Meng, C. H. Streuli, Circadian clocks and breast cancer. *Breast Cancer Res* **18**, 89 (2016).
12. E. S. Schernhammer, F. Laden, F. E. Speizer, W. C. Willett, D. J. Hunter, I. Kawachi, G. A. Colditz, Rotating night shifts and risk of breast cancer in women participating in the nurses' health study. *J Natl Cancer Inst* **93**, 1563-1568 (2001).
13. P. Alluri, L. A. Newman, Basal-Like and Triple-Negative Breast Cancers: Searching for Positives Among Many Negatives. *Surgical Oncology Clinics of North America* **23**, 567-577 (2014).
14. C. Anders, L. A. Carey, Understanding and treating triple-negative breast cancer. *Oncology (Williston Park)* **22**, 1233-1239; discussion 1239-1240, 1243 (2008).

15. N. M. Almansour, Triple-Negative Breast Cancer: A Brief Review About Epidemiology, Risk Factors, Signaling Pathways, Treatment and Role of Artificial Intelligence. *Front Mol. Biosci* **9**, (2022).
16. J. A. Mohawk, C. B. Green, J. S. Takahashi, Central and peripheral circadian clocks in mammals. *Annu Rev Neurosci* **35**, 445-462 (2012).
17. C. M. McQueen, E. E. Schmitt, T. R. Sarkar, J. Elswood, R. P. Metz, D. Earnest, M. Rijnkels, W. W. Porter, PER2 regulation of mammary gland development. *Development* **145**, (2018).
18. M. H. Vitaterna, K. Shimomura, P. Jiang, Genetics of Circadian Rhythms. *Neurol Clin* **37**, 487-504 (2019).
19. E. M. Stephenson, L. E. J. Usselmann, V. Tergaonkar, D. M. Virshup, R. Dallmann, Cancer clocks in tumourigenesis: the p53 pathway and beyond. *Endocrine-Related Cancer* **28**, R95-R110 (2021).
20. F. Battaglin, P. Chan, Y. Pan, S. Soni, M. Qu, E. R. Spiller, S. Castanon, E. T. Roussos Torres, S. M. Mumenthaler, S. A. Kay, H.-J. Lenz, Clocking cancer: the circadian clock as a target in cancer therapy. *Oncogene* **40**, 3187-3200 (2021).
21. X. Yuan, C. Zhu, M. Wang, F. Mo, W. Du, X. Ma, Night Shift Work Increases the Risks of Multiple Primary Cancers in Women: A Systematic Review and Meta-analysis of 61 Articles. *Cancer Epidemiol Biomarkers Prev* **27**, 25-40 (2018).
22. N. Sharma, Atolagbe, O., Ge, Z., Allison, J, LILRB4 suppresses immunity in solid tumors and is a potential target for immunotherapy. *J of Exp Medicine* **218**, (2021).
23. M. Deng, X. Gui, J. Kim, L. Xie, W. Chen, Z. Li, L. He, Y. Chen, H. Chen, W. Luo, Z. Lu, J. Xie, H. Churchill, Y. Xu, Z. Zhou, G. Wu, C. Yu, S. John, K. Hirayasu, N. Nguyen, X. Liu, F. Huang, L. Li, H. Deng, H. Tang, A. H. Sadek, L. Zhang, T. Huang, Y. Zou, B. Chen, H. Zhu, H. Arase, N. Xia, Y. Jiang, R. Collins, M. J. You, J. Homsi, N. Unni, C. Lewis, G. Q. Chen, Y. X. Fu, X. C. Liao, Z. An, J. Zheng, N. Zhang, C. C. Zhang, LILRB4 signalling in leukaemia cells mediates T cell suppression and tumour infiltration. *Nature* **562**, 605-609 (2018).
24. S. Lee, L. A. Donehower, A. J. Herron, D. D. Moore, L. Fu, Disrupting circadian homeostasis of sympathetic signaling promotes tumor development in mice. *PLoS One* **5**, e10995 (2010).
25. I. G. Maroulakou, M. Anver, L. Garrett, J. E. Green, Prostate and mammary adenocarcinoma in transgenic mice carrying a rat C3(1) simian virus 40 large tumor antigen fusion gene. *Proc Natl Acad Sci U S A* **91**, 11236-11240 (1994).
26. J. Usary, Darr, UB., Pfefferle, A, Perou, C., Genetically Engineered Mouse Models of Distinct Breast Cancer Subtypes. *Curr Protoc Pharmacol* **72**, 38.31-38.11 (2017).
27. J. He, H. Pan, W. Liang, D. Xiao, X. Chen, M. Guo, J. He, Prognostic Effect of Albumin-to-Globulin Ratio in Patients with solid tumors: A Systematic Review and Meta-analysis. *J Cancer* **8**, 4002-4010 (2017).
28. C. W. Elston, I. O. Ellis, Pathological prognostic factors in breast cancer. I. The value of histological grade in breast cancer: experience from a large study with long-term follow-up. *Histopathology* **41**, 154-161 (2002).
29. J. S. Meyer, S. E. Howden, K. A. Wallace, A. D. Verhoeven, L. S. Wright, E. E. Capowski, I. Pinilla, J. M. Martin, S. Tian, R. Stewart, B. Pattnaik, J. A. Thomson, D. M. Gamm, Optic

vesicle-like structures derived from human pluripotent stem cells facilitate a customized approach to retinal disease treatment. *Stem Cells* **29**, 1206-1218 (2011).
30. M. Binnewies, E. W. Roberts, K. Kersten, V. Chan, D. F. Fearon, M. Merad, L. M. Coussens, D. I. Gabrilovich, S. Ostrand-Rosenberg, C. C. Hedrick, R. H. Vonderheide, M. J. Pittet, R. K. Jain, W. Zou, T. K. Howcroft, E. C. Woodhouse, R. A. Weinberg, M. F. Krummel, Understanding the tumor immune microenvironment (TIME) for effective therapy. *Nat Med* **24**, 541-550 (2018).
31. P. Sangwung, G. Zhou, L. Nayak, E. R. Chan, S. Kumar, D. W. Kang, R. Zhang, X. Liao, Y. Lu, K. Sugi, H. Fujioka, H. Shi, S. D. Lapping, C. C. Ghosh, S. J. Higgins, S. M. Parikh, H. Jo, M. K. Jain, KLF2 and KLF4 control endothelial identity and vascular integrity. *JCI Insight* **2**, e91700 (2017).
32. Y. Wang, K. Wang, H. Zhang, X. Jia, X. Li, S. Sun, D. Sun, Cell death-related biomarker SLC2A1 has a significant role in prognosis prediction and immunotherapy efficacy evaluation in pan-cancer. *Frontiers in Genetics* **13**, (2023).
33. D. Ai, J. Yao, F. Yang, L. Huo, H. Chen, W. Lu, L. M. S. Soto, M. Jiang, M. G. Raso, S. Wang, D. Bell, J. Liu, H. Wang, D. Tan, C. Torres-Cabala, Q. Gan, Y. Wu, C. Albarracin, M.-C. Hung, F. Meric-Bernstam, I. I. Wistuba, V. G. Prieto, A. A. Sahin, Q. Ding, TRPS1: a highly sensitive and specific marker for breast carcinoma, especially for triple-negative breast cancer. *Modern Pathology* **34**, 710-719 (2021).
34. E. Neubauer, R. M. Wirtz, D. Kaemmerer, M. Athelogou, L. Schmidt, J. Sanger, A. Lupp, Comparative evaluation of three proliferation markers, Ki-67, TOP2A, and RacGAP1, in bronchopulmonary neuroendocrine neoplasms: Issues and prospects. *Oncotarget* **7**, 41959-41973 (2016).
35. A. C. Moreira, T. Silva, G. Mesquita, A. C. Gomes, C. M. Bento, J. V. Neves, D. F. Rodrigues, P. N. Rodrigues, A. A. Almeida, P. Santambrogio, M. S. Gomes, H-Ferritin Produced by Myeloid Cells Is Released to the Circulation and Plays a Major Role in Liver Iron Distribution during Infection. *International Journal of Molecular Sciences* **23**, 10.3390/ijms23010269 (2022).
36. A. Bernal, L. Arranz, Nestin-expressing progenitor cells: function, identity and therapeutic implications. *Cell Mol Life Sci* **75**, 2177-2195 (2018).
37. D. Merrick, A. Sakers, Z. Irgebay, C. Okada, C. Calvert, M. P. Morley, I. Percec, P. Seale, Identification of a mesenchymal progenitor cell hierarchy in adipose tissue. *Science* **364**, (2019).
38. F. Fei, J. Qu, C. Li, X. Wang, Y. Li, S. Zhang, Role of metastasis-induced protein S100A4 in human non-tumor pathophysiologies. *Cell Biosci* **7**, 64 (2017).
39. G. Wu, Sun, D., Liao, Y., Shang, K., Lu, C., RPL35A is a key promotor involved in the development and progression of gastric cancer. *Cancer Cell International* **21**, (2021).
40. M. Li, T. Nishimura, Y. Takeuchi, T. Hongu, Y. Wang, D. Shiokawa, K. Wang, H. Hirose, A. Sasahara, M. Yano, S. Ishikawa, M. Inokuchi, T. Ota, M. Tanabe, K. I. Tada, T. Akiyama, X. Cheng, C. C. Liu, T. Yamashita, S. Sugano, Y. Uchida, T. Chiba, H. Asahara, M. Nakagawa, S. Sato, Y. Miyagi, T. Shimamura, L. A. E. Nagai, A. Kanai, M. Katoh, S. Nomura, R. Nakato, Y. Suzuki, A. Tojo, D. C. Voon, S. Ogawa, K. Okamoto, T. Foukakis, N. Gotoh, FXYD3 functionally demarcates an ancestral breast cancer stem cell subpopulation with features of drug-tolerant persisters. *J Clin Invest* **133**, (2023).

41. H. Strobl, C. Scheinecker, E. Riedl, B. Csmarits, C. Bello-Fernandez, W. F. Pickl, O. Majdic, W. Knapp, Identification of CD68+lin− Peripheral Blood Cells with Dendritic Precursor Characteristics1. *The Journal of Immunology* **161**, 740-748 (1998).
42. C. Han, T. Liu, R. Yin, Biomarkers for cancer-associated fibroblasts. *Biomark Res* **8**, 64 (2020).
43. M. Trzpis, P. M. McLaughlin, L. M. de Leij, M. C. Harmsen, Epithelial cell adhesion molecule: more than a carcinoma marker and adhesion molecule. *Am J Pathol* **171**, 386-395 (2007).
44. S. J. Baker, P. I. Poulikakos, H. Y. Irie, S. Parekh, E. P. Reddy, CDK4: a master regulator of the cell cycle and its role in cancer. *Genes Cancer* **13**, 21-45 (2022).
45. L. Grosche, I. Knippertz, C. Konig, D. Royzman, A. B. Wild, E. Zinser, H. Sticht, Y. A. Muller, A. Steinkasserer, M. Lechmann, The CD83 Molecule - An Important Immune Checkpoint. *Front Immunol* **11**, 721 (2020).
46. X. Ren, S. Guo, X. Guan, Y. Kang, J. Liu, X. Yang, Immunological Classification of Tumor Types and Advances in Precision Combination Immunotherapy. *Front Immunol* **13**, 790113 (2022).
47. A. E. Vilgelm, A. Richmond, Chemokines Modulate Immune Surveillance in Tumorigenesis, Metastasis, and Response to Immunotherapy. *Frontiers in Immunology* **10**, (2019).
48. Z. Yang, L., Liu, K.Y., Lin, F.J., Shi, H.M., Ou, Z.L., CCL28 promotes breast cancer growth and metastasis through MAPK-mediated cellular anti-apoptosis and pro-metastasis. *Oncology Reports* **38**, 1393-1401 (2017).
49. S. Z. Wu, G. Al-Eryani, D. L. Roden, S. Junankar, K. Harvey, A. Andersson, A. Thennavan, C. Wang, J. R. Torpy, N. Bartonicek, T. Wang, L. Larsson, D. Kaczorowski, N. I. Weisenfeld, C. R. Uytingco, J. G. Chew, Z. W. Bent, C.-L. Chan, V. Gnanasambandapillai, C.-A. Dutertre, L. Gluch, M. N. Hui, J. Beith, A. Parker, E. Robbins, D. Segara, C. Cooper, C. Mak, B. Chan, S. Warrier, F. Ginhoux, E. Millar, J. E. Powell, S. R. Williams, X. S. Liu, S. O'Toole, E. Lim, J. Lundeberg, C. M. Perou, A. Swarbrick, A single-cell and spatially resolved atlas of human breast cancers. *Nat Genet* **53**, 1334-1347 (2021).
50. I. Tirosh, B. Izar, S. M. Prakadan, M. H. Wadsworth, 2nd, D. Treacy, J. J. Trombetta, A. Rotem, C. Rodman, C. Lian, G. Murphy, M. Fallahi-Sichani, K. Dutton-Regester, J. R. Lin, O. Cohen, P. Shah, D. Lu, A. S. Genshaft, T. K. Hughes, C. G. Ziegler, S. W. Kazer, A. Gaillard, K. E. Kolb, A. C. Villani, C. M. Johannessen, A. Y. Andreev, E. M. Van Allen, M. Bertagnolli, P. K. Sorger, R. J. Sullivan, K. T. Flaherty, D. T. Frederick, J. Jane-Valbuena, C. H. Yoon, O. Rozenblatt-Rosen, A. K. Shalek, A. Regev, L. A. Garraway, Dissecting the multicellular ecosystem of metastatic melanoma by single-cell RNA-seq. *Science* **352**, 189-196 (2016).
51. L. He, Y. Fan, Y. Zhang, T. Tu, Q. Zhang, F. Yuan, C. Cheng, Single-cell transcriptomic analysis reveals circadian rhythm disruption associated with poor prognosis and drug-resistance in lung adenocarcinoma. *J Pineal Res* **73**, e12803 (2022).
52. F. Behbod, A. M. Gomes, H. L. Machado, Modeling Human Ductal Carcinoma In Situ in the Mouse. *J Mammary Gland Biol Neoplasia* **23**, 269-278 (2018).
53. M. Szkiela, Kusidel, E., Dabrowska, TM, Kaleta, D. , How the Intensity of Night Shift Work Affects Breast Cancer Risk. *IJERPH* **18**, (2021).

54. A. Labani-Motlagh, M. Ashja-Mahdavi, A. Loskog, The Tumor Microenvironment: A Milieu Hindering and Obstructing Antitumor Immune Responses. *Front Immunol* **11**, 940 (2020).
55. A. M. Yang J, Ling S, Teitz-Tennenbaum S, Zemans RL, Osterholzer JJ, Sisson TH, Kim KK., Diverse Injury Pathways Induce Alveolar Epithelial Cell CCL2/12, Which Promotes Lung Fibrosis. *Am J Respir Cell Mol Biol.* **62**, 622-632 (2020).
56. K. Li, H. Shi, B. Zhang, X. Ou, Q. Ma, Y. Chen, P. Shu, D. Li, Y. Wang, Myeloid-derived suppressor cells as immunosuppressive regulators and therapeutic targets in cancer. *Signal Transduction and Targeted Therapy* **6**, 362 (2021).
57. L. Ren, Y. Yu, L. Wang, Z. Zhu, R. Lu, Z. Yao, Hypoxia-induced CCL28 promotes recruitment of regulatory T cells and tumor growth in liver cancer. *Oncotarget* **7**, 75763-75773 (2016).
58. C. Wang, C. Barnoud, M. Cenerenti, M. Sun, I. Caffa, B. Kizil, R. Bill, Y. Liu, R. Pick, L. Garnier, O. A. Gkountidi, L. M. Ince, S. Holtkamp, N. Fournier, O. Michielin, D. E. Speiser, S. Hugues, A. Nencioni, M. J. Pittet, C. Jandus, C. Scheiermann, Dendritic cells direct circadian anti-tumour immune responses. *Nature* **614**, 136-143 (2023).
59. A. Costa, Y. Kieffer, A. Scholer-Dahirel, F. Pelon, B. Bourachot, M. Cardon, P. Sirven, I. Magagna, L. Fuhrmann, C. Bernard, C. Bonneau, M. Kondratova, I. Kuperstein, A. Zinovyev, A.-M. Givel, M.-C. Parrini, V. Soumelis, A. Vincent-Salomon, F. Mechta-Grigoriou, Fibroblast Heterogeneity and Immunosuppressive Environment in Human Breast Cancer. *Cancer Cell* **33**, 463-479.e410 (2018).
60. I. Aiello, M. L. M. Fedele, F. Roman, L. Marpegan, C. Caldart, J. J. Chiesa, D. A. Golombek, C. V. Finkielstein, N. Paladino, Circadian disruption promotes tumor-immune microenvironment remodeling favoring tumor cell proliferation. *Sci Adv* **6**, (2020).
61. N. B. Hao, M. H. Lu, Y. H. Fan, Y. L. Cao, Z. R. Zhang, S. M. Yang, Macrophages in tumor microenvironments and the progression of tumors. *Clin Dev Immunol* **2012**, 948098 (2012).
62. Y. Pan, Y. Yu, X. Wang, T. Zhang, Tumor-Associated Macrophages in Tumor Immunity. *Front Immunol* **11**, 583084 (2020).
63. S. M. Wong YL, Sugahara-Tobinai A, Itoi S, Kezuka D, Endo S, Inui M, Takai T. , Gp49B is a pathogenic marker for auto-antibody-producing plasma cells in lupus-prone BXSB/Yaa mice. *Int Immunol* **31**, 397–406 (2019).
64. W. van der Touw, H. M. Chen, P. Y. Pan, S. H. Chen, LILRB receptor-mediated regulation of myeloid cell maturation and function. *Cancer Immunol Immunother* **66**, 1079-1087 (2017).
65. A. Waschbisch, N. Sanderson, M. Krumbholz, G. Vlad, D. Theil, S. Schwab, M. Maurer, T. Derfuss, Interferon beta and vitamin D synergize to induce immunoregulatory receptors on peripheral blood monocytes of multiple sclerosis patients. *PLoS One* **9**, e115488 (2014).
66. A. D. Truong, Y. Hong, H. T. T. Tran, H. V. Dang, V. K. Nguyen, T. T. Pham, H. S. Lillehoj, Y. H. Hong, Characterization and functional analyses of novel chicken leukocyte immunoglobulin-like receptor subfamily B members 4 and 5. *Poult Sci* **98**, 6989-7002 (2019).

67. Z. Xu, C. C. Chang, M. Li, Q. Y. Zhang, E. M. Vasilescu, V. D'Agati, A. Floratos, G. Vlad, N. Suciu-Foca, ILT3.Fc-CD166 Interaction Induces Inactivation of p70 S6 Kinase and Inhibits Tumor Cell Growth. *J Immunol* **200**, 1207-1219 (2018).
68. P. L. de Goeje, K. Bezemer, M. E. Heuvers, A.-M. C. Dingemans, H. J. Groen, E. F. Smit, H. C. Hoogsteden, R. W. Hendriks, J. G. Aerts, J. P. Hegmans, Immunoglobulin-like transcript 3 is expressed by myeloid-derived suppressor cells and correlates with survival in patients with non-small cell lung cancer. *OncoImmunology* **4**, e1014242 (2015).
69. X. Gui, M. Deng, H. Song, Y. Chen, J. Xie, Z. Li, L. He, F. Huang, Y. Xu, Y. Anami, H. Yu, C. Yu, L. Li, Z. Yuan, X. Xu, Q. Wang, Y. Chai, T. Huang, Y. Shi, K. Tsuchikama, X. C. Liao, N. Xia, G. F. Gao, N. Zhang, C. C. Zhang, Z. An, Disrupting LILRB4/APOE Interaction by an Efficacious Humanized Antibody Reverses T-cell Suppression and Blocks AML Development. *Cancer Immunol Res* **7**, 1244-1257 (2019).
70. C. C. Chang, Z. Liu, G. Vlad, H. Qin, X. Qiao, D. M. Mancini, C. C. Marboe, R. Cortesini, N. Suciu-Foca, Ig-like transcript 3 regulates expression of proinflammatory cytokines and migration of activated T cells. *J Immunol* **182**, 5208-5216 (2009).
71. A. Sugahara-Tobinai, M. Inui, T. Metoki, Y. Watanabe, R. Onuma, T. Takai, S. Kumaki, Augmented ILT3/LILRB4 Expression of Peripheral Blood Antibody Secreting Cells in the Acute Phase of Kawasaki Disease. *Pediatr Infect Dis J* **38**, 431-438 (2019).
72. X. Sun, D. J. Glynn, L. J. Hodson, C. Huo, K. Britt, E. W. Thompson, L. Woolford, A. Evdokiou, J. W. Pollard, S. A. Robertson, W. V. Ingman, CCL2-driven inflammation increases mammary gland stromal density and cancer susceptibility in a transgenic mouse model. *Breast Cancer Res* **19**, 4 (2017).
73. P. Shu Kurizky, L. L. Dos Santos Neto, R. Barbosa Aires, L. M. Henrique da Mota, C. Martins Gomes, Opportunistic tropical infections in immunosuppressed patients. *Best Pract Res Clin Rheumatol* **34**, 101509 (2020).
74. L. P. Casiraghi, G. A. Oda, J. J. Chiesa, W. O. Friesen, D. A. Golombek, Forced Desynchronization of Activity Rhythms in a Model of Chronic Jet Lag in Mice. *Journal of Biological Rhythms* **27**, 59-69 (2012).
75. B. Schmid, C. Helfrich-Förster, T. Yoshii, A New ImageJ Plug-in “ActogramJ” for Chronobiological Analyses. *Journal of Biological Rhythms* **26**, 464-467 (2011).
76. S. Yang, J. J. Zhang, X.-Y. Huang, "Mouse Models for Tumor Metastasis" in *Rational Drug Design: Methods and Protocols,* Y. Zheng, Ed. (Humana Press, Totowa, NJ, 2012), pp. 221-228.
77. V. Kersemans, B. Cornelissen, P. D. Allen, J. S. Beech, S. C. Smart, Subcutaneous tumor volume measurement in the awake, manually restrained mouse using MRI. *Journal of Magnetic Resonance Imaging* **37**, 1499-1504 (2013).
78. G. Finak, A. McDavid, M. Yajima, J. Deng, V. Gersuk, A. K. Shalek, C. K. Slichter, H. W. Miller, M. J. McElrath, M. Prlic, P. S. Linsley, R. Gottardo, MAST: a flexible statistical framework for assessing transcriptional changes and characterizing heterogeneity in single-cell RNA sequencing data. *Genome Biology* **16**, 278 (2015).
79. T. Wu, E. Hu, S. Xu, M. Chen, P. Guo, Z. Dai, T. Feng, L. Zhou, W. Tang, L. Zhan, X. Fu, S. Liu, X. Bo, G. Yu, clusterProfiler 4.0: A universal enrichment tool for interpreting omics data. *The Innovation* **2**, 100141 (2021).

80. Y. Hao, S. Hao, E. Andersen-Nissen, W. M. Mauck, S. Zheng, A. Butler, M. J. Lee, A. J. Wilk, C. Darby, M. Zager, P. Hoffman, M. Stoeckius, E. Papalexi, E. P. Mimitou, J. Jain, A. Srivastava, T. Stuart, L. M. Fleming, B. Yeung, A. J. Rogers, J. M. McElrath, C. A. Blish, R. Gottardo, P. Smibert, R. Satija, Integrated analysis of multimodal single-cell data. *Cell* **184**, 3573-3587.e3529 (2021).

Acknowledgments
We thank Dr. Mahul Chakraborty for helping with real-time PCR, Dr. Gus Wright for helping with flow cytometry experiments and analysis, our histology core facility (Texas A&M University) for helping with tumor and mammary gland histology, Ashley Nguyen, David Arreola, Subiksha Sankar, and Aaryan Amin for helping with circadian cabinets.

Funding: This work was funded by the Texas A&M University Faculty Development Grant (to T.R.S) and Strategic Transformative Research Funds (STRP to TRS), NIH grant NIH 5 P01HL160471 (to A.K) and NIH R01NS131628 (to A.K), NIH R35GM151020 (to J.J), and NSF CCF-1934904 (to B.M).

Author contributions: Conceptualization: T.R.S. Methodology: O.O., M.S., A.C, D.J.B., T.N., D.F., Y.J-H., J.J and T.R.S. Investigation: O.O., M.S., A.C, D.J.B., T.N., T.R.S. Visualization: O.O, M.S., D.F., YJ-H., T.R.S. Supervision: T.R.S. Analysis of data: T.R.S., B.M., J.J., A.K. Writing—original draft: O.O., M.S., T.R.S. Review and editing: A.K., B.M., L.F and J.J.

Competing interests: Authors declare that they have no competing interests.

Data and materials availability: All data needed to evaluate the conclusions in the paper are present in the paper and/or the Supplementary Materials.

Figures

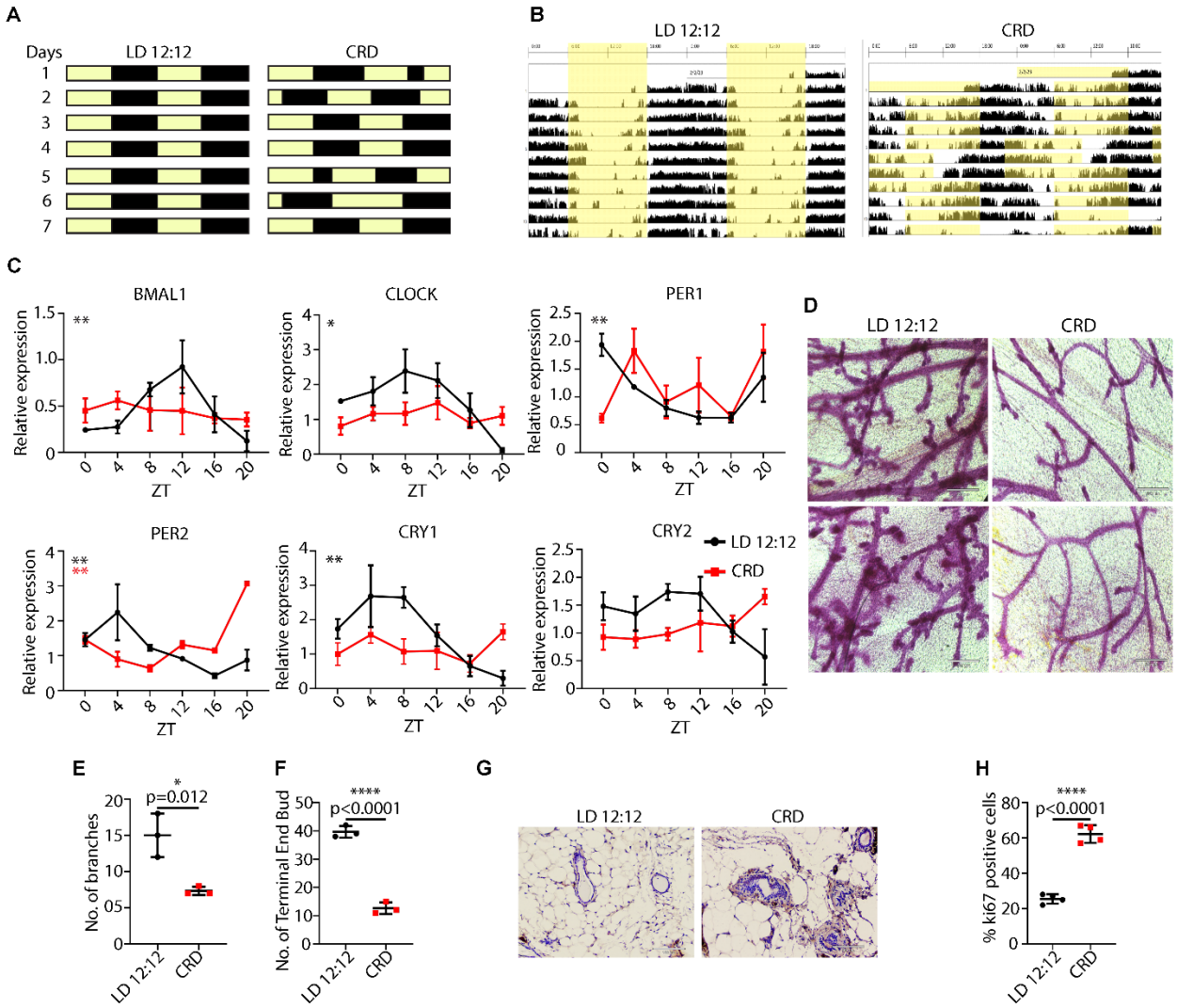

Fig. 1. CRD severely impairs rhythmicity and disrupts mammary gland morphogenesis. (A) Schematic representation of the CRD protocol. **(B)** FVB female mice were housed under LD 12:12 or CRD for 8 weeks. Representative actograms of LD and CRD mice. LD: 12 h light and 12 h dark; CRD: circadian rhythm disruption using jet lag protocol, represented by a shortening of the dark period by 8 h every third day. **(C)** Mammary glands were collected at the indicated times. Gene expression normalized to GAPDH expression was measured using quantitative real-time PCR data represented as mean ± SEM for n=4 females per time point and light condition. Rhythmicity was determined using JTK_Cycle analyses; **P*JTKcycle < 0.05, ***P*JTKcycle < 0.01, ****P*JTKcycle < 0.001, and *****P*JTKcycle < 0.0001. CRD disrupts branching morphogenesis in WT virgin FVB mice. **(D, E, F)** Representative images of branching and development of terminal ducts in LD and CRD animals are shown in LD and CRD-induced mammary glands **(D, E, F)**, scale bar: 350 µm, (**P* < 0.05, error bars indicate SEM, n = 4). **(G)** The effect of CRD on mammary ductal hyperplasia is shown by hematoxylin and eosin (H&E) staining of the mammary gland (**G**) and by using Ki67 **(H)** of the mammary glands. Scale bar: 100 µm.

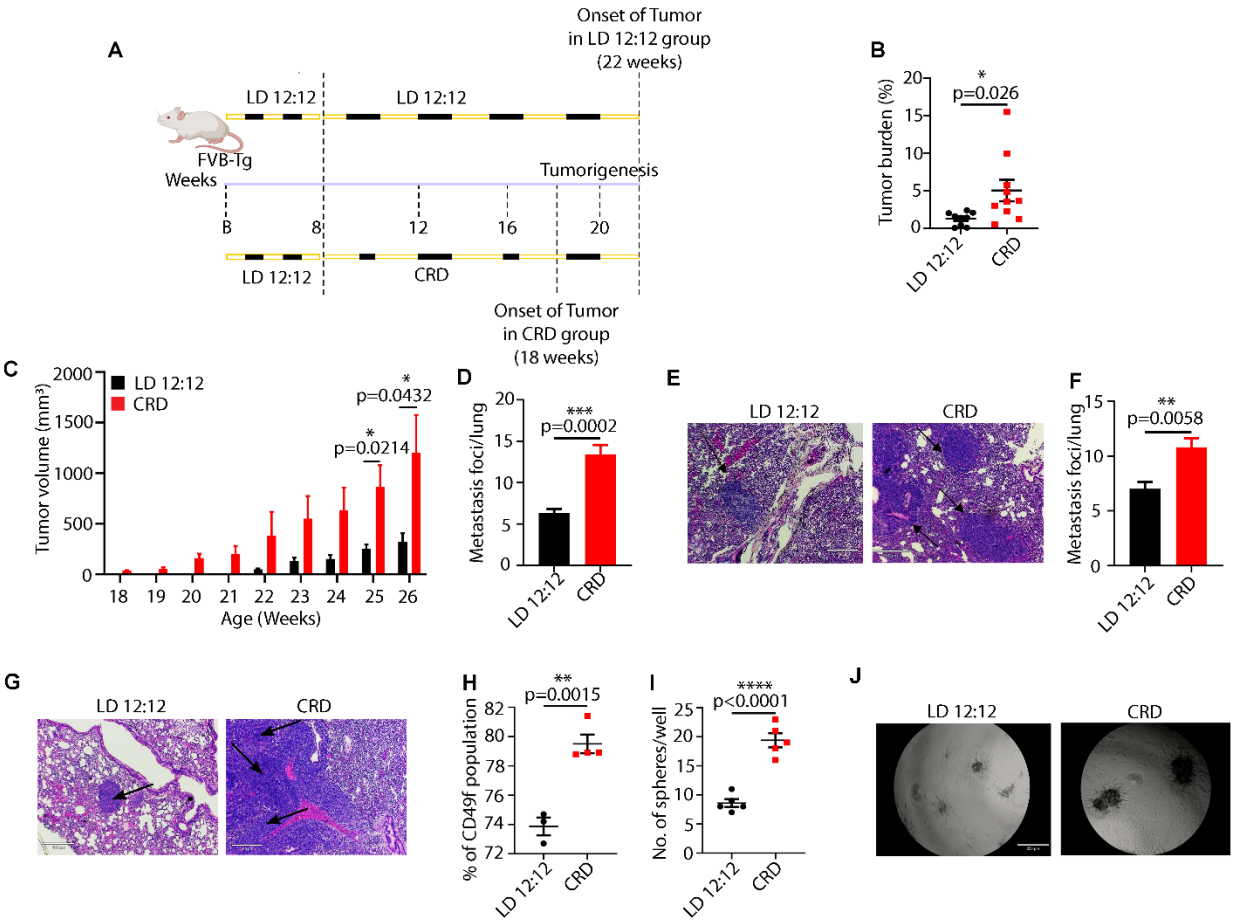

Fig. 2. CRD increases aggressive mammary tumorigenesis and lung metastasis. Experimental timeline for evaluation of the effect of CRD on spontaneous TNBC in (FVB-Tg(C3-1-TAg)cJeg (C3-TAg) mice **(A)**. Dashed lines highlight the start and end points of the experiment. **(B)** Tumor burden (tumor to body weight ratio) as % in LD (n = 9) or CRD (n = 10) conditions. Column data represent the mean ± SEM values for individual animals. The effect of CRD on tumor initiation is shown in **(C)**. Number of metastatic foci in the lungs of LD (n=6) and CRD (n =7) mice at the time of their sacrifice is shown in **(D)**. P-value obtained from a binomial two-sided test. Indicated (n) represents the number of independent experiments as biological replicates. Metastatic foci in the lungs are shown using H&E staining, scale bar 150 µm **(E)**. CRD-induced lung metastasis in 4T1 tumor model in BALB/cJ mice as shown by the graphical representation **(F)** and H&E staining **(G),** scale bar 100 µm. **(H)** The percentage of CD49f-breast cancer stem cell (CSC) subpopulations in LD and CRD tumors is shown as a graph. Results represent the mean ± SEM of 3–4 independent experiments. P-value obtained from an unpaired two-sided *t*-test. Mammosphere formation efficiency (MFE%) of LD and CRD tumor cells (n =3) is shown in Figure. **(I)** with lines indicating the mean ± SEM. P-value obtained from an unpaired two-sided *t*-test. The formation of organoids (tumoroids) from LD and CRD tumors is shown in the **J**. Scale bar, 250 µm.

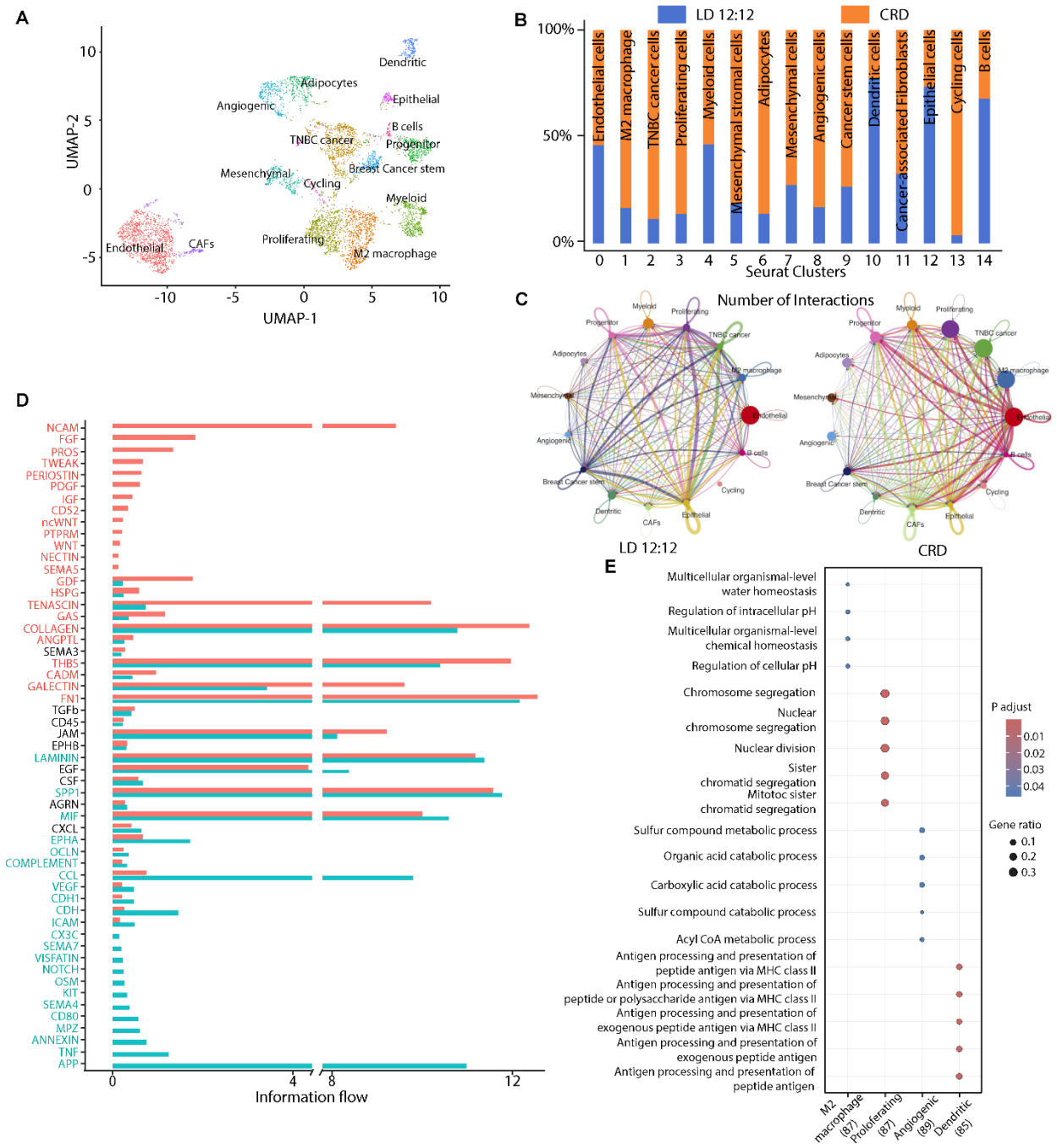

Fig. 3. CRD alters the tumor microenvironment. Cell clusters from 10x Genomics scRNA-seq analysis visualized using Uniform Manifold Approximation (UMAP). Colors indicate clusters of various cell types **(A)**. Fraction of cells from tumors (LD and CRD) in each cluster **(B)**. Clusters were annotated for their cell types as predicted using canonical markers and signature-based annotation with Garnett. Expression markers for endothelial cells (*KLF2*), M2 macrophages (*SLC2A1*), TNBC cancer cells (*TRPS1*), proliferating cells (*TOP2A)*, myeloid cells (*FTH1)*, progenitor cells (*NES*), adipocytes (*CLEC11A*), mesenchymal cells (*S100A4*), angiogenic cells (*RPL35A*), breast cancer stem cells *(FXYD3*), dendritic cells (*CD68*), cancer-associated fibroblast (*COL1A2*), epithelial cells (*EPCAM*), cycling cells (*CDK4*), and B-cells (*CD83*). The comparison of the total number of interactions among different cell populations between LD and CRD tumors

is shown in **C**. Edge width is proportional to the number of interactions, which assesses the number of ligand–receptor pairs contributing to the communication between two interacting cell populations. CellChat analysis quantitatively analyzes intercellular communication networks **(D)**. The analysis shows differential ligand–receptor interactions between LD and CRD tumors. Significant signaling pathways were ranked based on differences in the information flow within the inferred networks between LD and CRD tumors. Dot plot profiling of the Gene Ontology (GO) analyses in each cluster **(E)**. The dot plot represents the average expression of GOs per cluster. The color gradient of dots represents the expression level, whereas the size represents the percentage of cells expressing any genes per cluster. The number indicates the total number of genes identified belonging to GO pathways significantly enriched in the cluster.

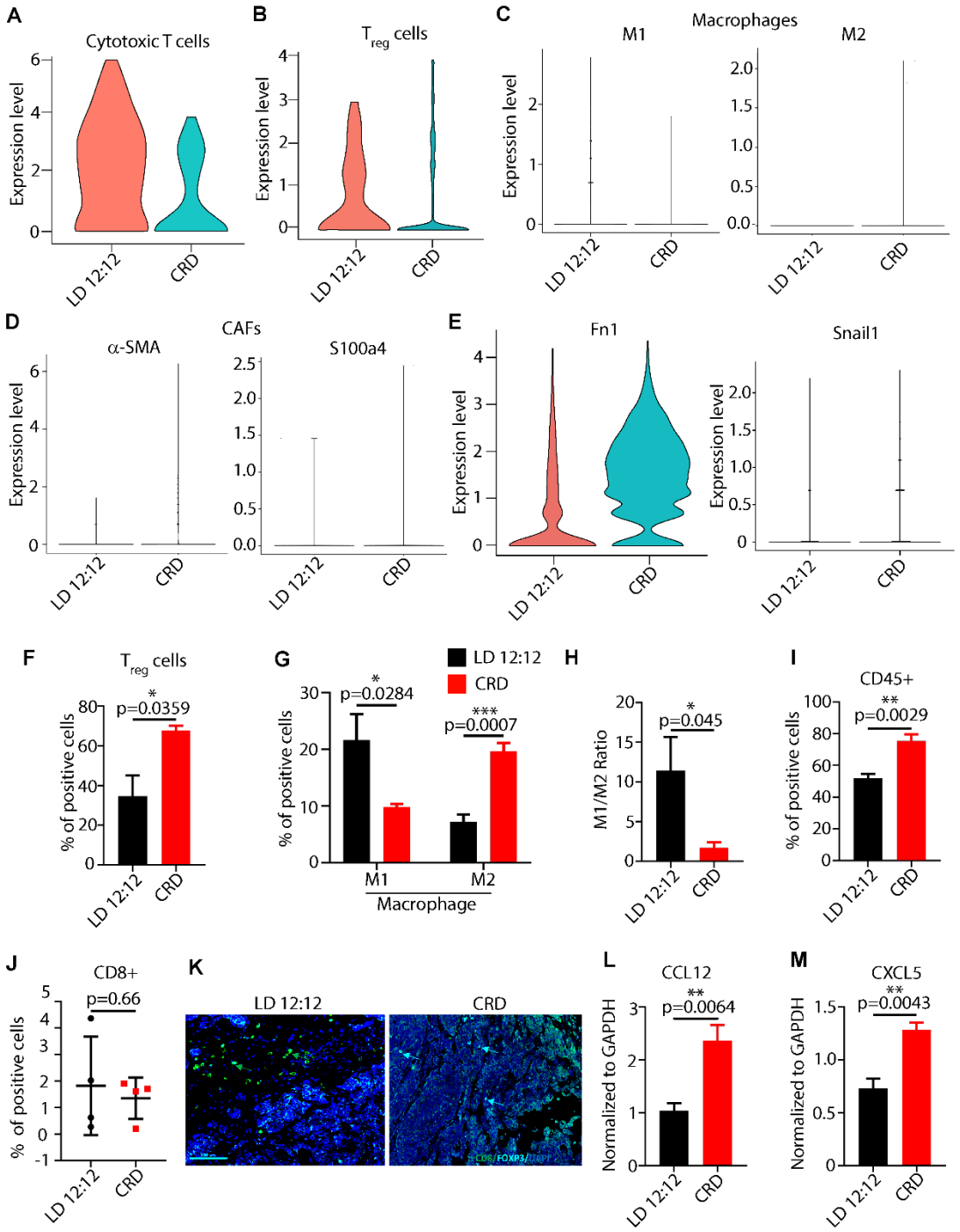

Fig. 4. CRD turns tumors "cold." Single-cell RNA seq (scRNA Seq) study showed the cytotoxic T cells **(A),** regulatory T cells (T_{reg}) **(B),** Macrophages (M1 and M2) **(C),** cancer-associated fibroblast (CAF) population based on S100a4, and α-SMA markers, and epithelial to mesenchymal (EMT) markers (Fibronectin and Snail1) **(E)** in LD and CRD-induced tumors. Flow cytometry revealed a significant increase in the $FoxP3^+$ T_{reg} population in the tumors of CRD mice (n = 4) **(F).** The percentage of antitumor M1 macrophage population and, pro-tumor M2 macrophage population (n =4) in LD and CRD-induced 4T1 tumors is shown in **(G),** and an overall ratio of M1/M2 is shown in **(H)**. The percentage of total leukocytes ($CD45^+$ cells) in LD and CRD-induced

tumors is shown in **(I)**. P-value obtained from an unpaired two-sided *t*-test. The percentage of cytotoxic T cells ($CD8^+$ T cells) in LD and CRD-induced tumors is shown in **(J)**. Representative multiplexing immunostaining image (MxIF) of cytotoxic CD8 T-cell (CD8, green), T_{reg} (FOXP3, cyan) in the LD and CRD-induced GEMM tumors (n = 4) Scale bar= 100µm **(K)**. The expression of chemokines CCL12 **(L)** and CXCL5 **(M),** is shown using real-time PCR in LD and CRD-induced tumors (n = 4).

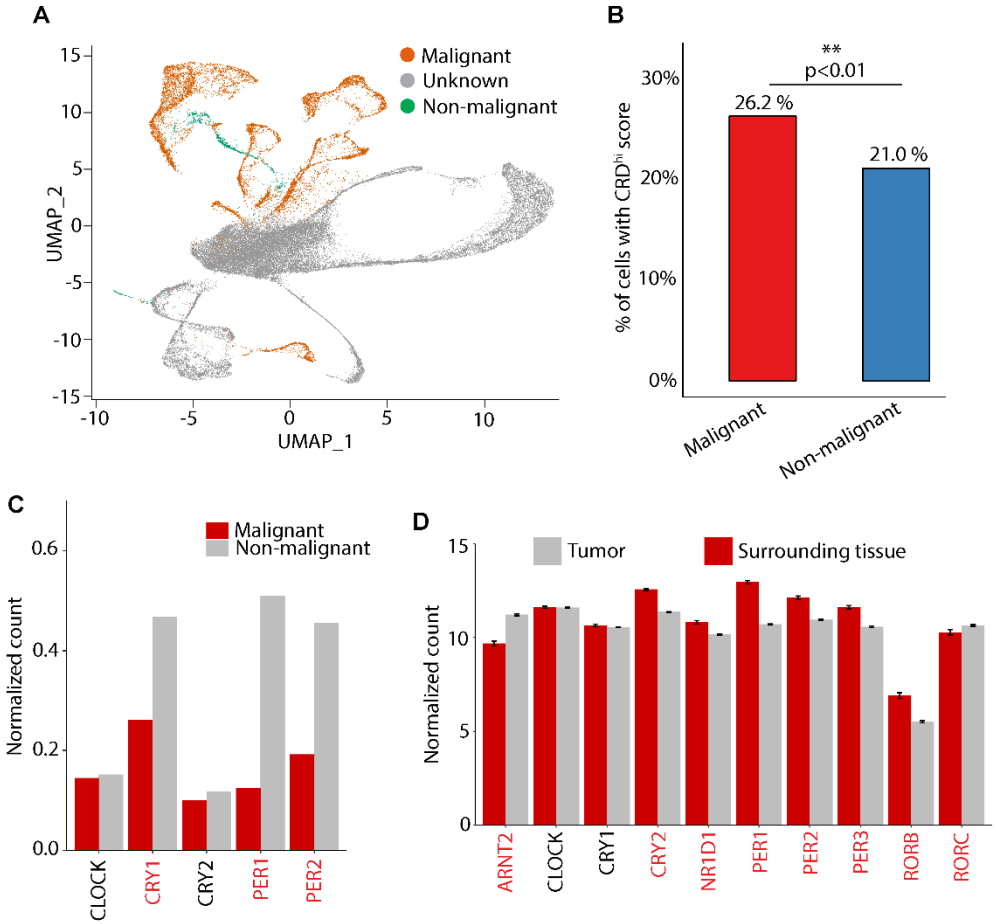

Fig. 5. The human circadian clock is disrupted in breast cancer. UMAP of malignant and nonmalignant cells (total cells = 42,512) captured across patients with (n = 9) triple-negative breast tumors. Moving from the plot in **A**, 30,719 cells had an unknown inferCNV call and 11,793 had a known inferCNV call. These 11,793 single cells were used for downstream analysis to detect "malignant" and "nonmalignant" cells. The percentage of malignant and nonmalignant cells with CRD^{high} is shown in **B**. The mean normalized expression values of the core circadian genes by the cell type (malignant and nonmalignant) are presented in **C**. Red represents significant changes in expression between malignant and nonmalignant cells. **(D)** The mean expression of the clock genes (+/- standard error of mean) over patients by the type of tissue analyzed in TNBC tumors (n = 1104) and surrounding tissue (n = 113) using TCGA.

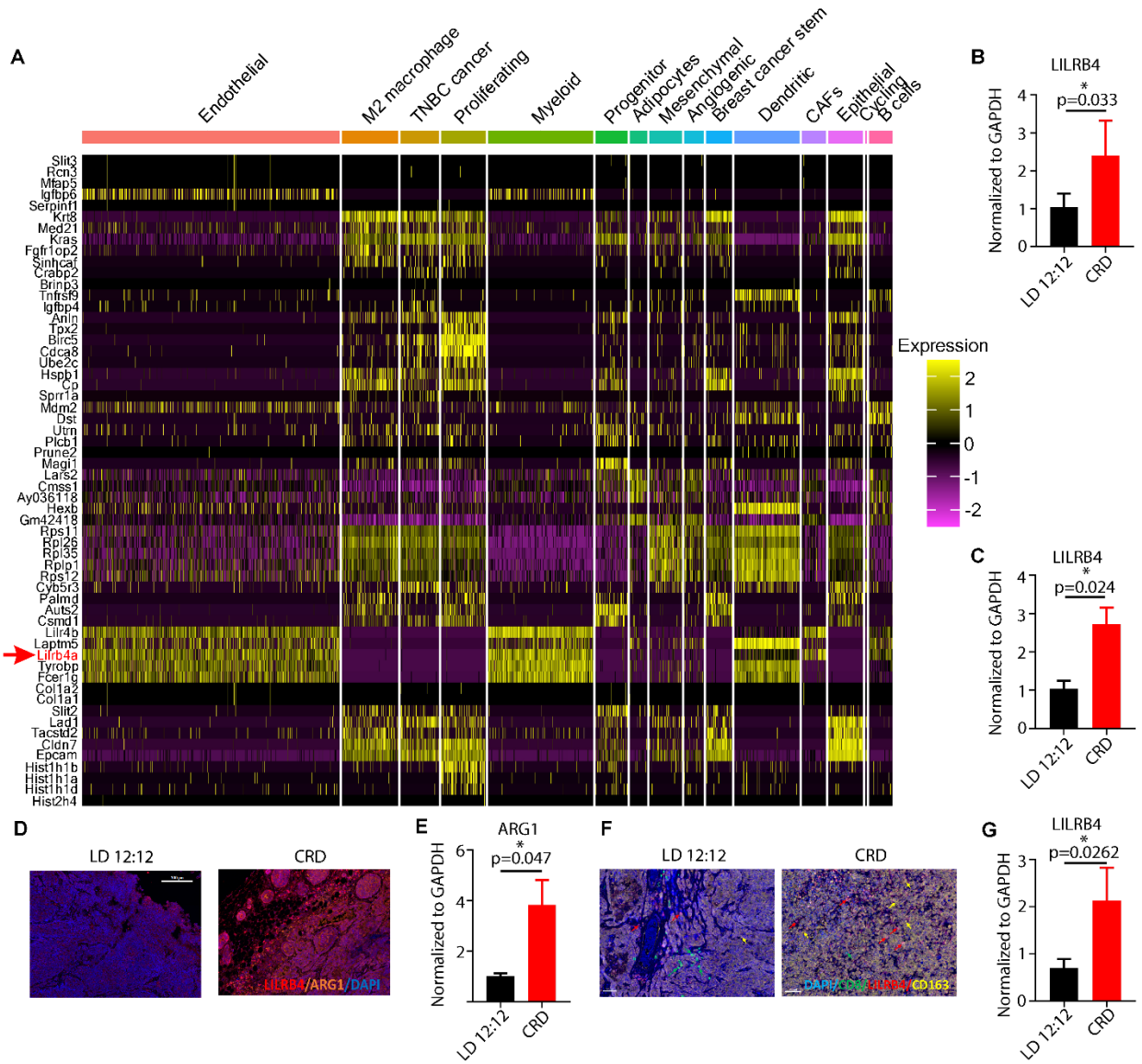

Fig. 6. CRD enhances LILRB4a expression to create an immunosuppressive tumor microenvironment. (A) Heatmaps of differentially expressed genes between LD 12:12 and CRD tumors identified using DESeq2 analyses of scRNA-seq. The transcript level of LILRB4 was analyzed in LD and CRD-induced GEMM tumors **(B)** and 4T1 tumors **(C)** using real-time PCR. **(D)** The expression of arginase 1 (ARG1, a downstream target of LILRB4a) was analyzed using immunofluorescence. Scale bar: 300µm **(E)** The transcript level of ARG1 in LD and CRD-induced GEMM tumors was analyzed using real-time PCR. **(F)** Representative MxIF showing the expression of LILRB4, CD8, CD163, and FOXP3 markers in LD and CRD-induced GEMM tumors. Scale bar: 50µm. **(G)** The transcript level of LILRB4 in LD and CRD-induced mammary glands was analyzed using real-time PCR.

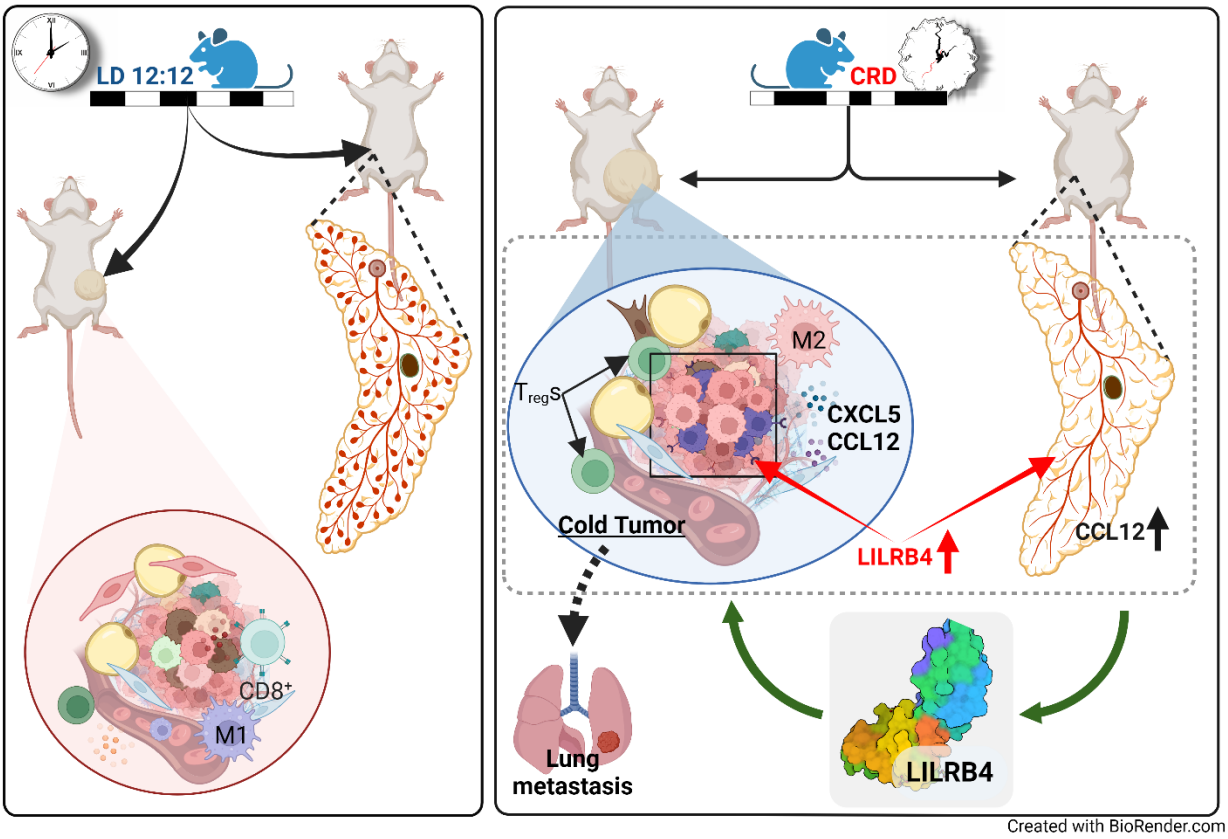

Fig 7. Diagrammatic representation of the molecular mechanism of CRD-induced immunosuppressive microenvironment in breast cancer. CRD enhances aggressive TNBC and lung metastasis by creating an immunosuppressive tumor microenvironment. CRD also disrupts the mammary gland morphology. Our study revealed that CRD enhanced LILRB4 expression, which induces an immunosuppressive "cold" TME by increasing the M2 macrophage and T_{reg} populations and decreasing M1 macrophage infiltration.